Inês Mendonça Lourenço Martins

Licenciada em Bioquímica

Effects of CORM-3 formulations in *in vitro* and *in vivo* models of inflammation

Dissertação para obtenção do Grau de Mestre em Química Bioorgânica

Orientador: Professora Doutora Teresa Sacadura Santos Silva
Co-orientador: Professora Doutora Maria Alexandra Núncio de Carvalho Ramos Fernandes

Júri
Presidente: Professora Doutora Paula Cristina de Sério Branco
Arguente: Professora Doutora Ana Isabel Tomaz
Vogal: Professora Doutora Teresa Sacadura Santos Silva

Março, 2020

FACULDADE DE CIÊNCIAS E TECNOLOGIA
UNIVERSIDADE NOVA DE LISBOA

Effects of CORM-3 formulations in *in vitro* and *in vivo* models of inflammation

ACKNOWLEDGMENTS

My first acknowledgment couldn't go to anyone but professor Teresa Santos Silva, my supervisor, for always being a helping hand. I will be forever grateful for all the trust and kindness you showed me since the very beginning and throughout this project. I also owe a special thank you to professor Alexandra Fernandes, my co-supervisor. Thank you for pushing me when I needed, for making me grow as a student and as a person. Additionally, I am thankful to professor Pedro Baptista for his advices and lab resources. I often forgot I wasn't officially under your supervision.

This journey wouldn't also be possible if it weren't for Bruno Vidal and his availability to teach. Thank you for your good mood, it made working in the weekend fun. There are many institutions, professors and colleagues who should be mentioned because in one way or another had an impact on my work. Given the risk of forgetting someone or significantly extending these words, I will only name Catarina Rodrigues and *Muthu*, and thank the others in this way, hoping they'll forgive me the anonymity.

It always takes some effort to adjust to a new place, so I was very lucky to have Beatriz Oliveira, Daniela Ferreira and Bruno Veigas who made it easy. Thank you, Bruno, for making me feel part of the "family", I hope you know what that meant to me. Thank you, Daniela, for all the food, parties and kind hostility, you made me smile every single day. Thank you, Beatriz, for all the conversations that got me through the lower times, I feel like we could cross the entire Lisbon on foot without realizing it.

Finally, I could never finish without thanking my parents for all the love, support and payment of my student debts. Thank you, *mãe*, for your ever-endless patience and, *pai*, for all the books.

RESUMO

As moléculas libertadoras de CO (CORMs) são uma nova classe de fármacos capazes de distribuir monóxido de carbono (CO) às células e tecidos de maneira controlada. Desta forma, mostram-se capazes de mimetizar os efeitos homeostáticos do CO gasoso em processos inflamatórios e sem os efeitos tóxicos que lhe são associados. A Molécula Libertadora de CO 3 (CORM-3) é um complexo carbonílico metálico de ruténio (Ru) capaz de libertar um dos seus ligandos sob a forma de CO quando em contacto com proteínas. Por estas razões, tem vindo a ser usada como molécula modelo para explorar o papel e as propriedades dos CORMs metálicos, tanto *in vitro* como *in vivo*.

A albumina é uma proteína central no transporte de drogas no sangue e, como tal, responsável pelo perfil farmacocinético e eficácia de muitos fármacos. Neste trabalho, análises espectroscópicas de UV-Vis e supressão (*quenching*) de fluorescência da albumina do soro bovina (BSA) na presença de CORM-3, mostram pequenas diferenças de conformação proteica após interação com o ligando e um efeito de *quenching* descrito pela relação de Stern-Volmer. A decomposição do CORM-3 no tampão fosfato usado caracteriza-se por uma constante de degradação de 0.0026 s^{-1} e um tempo de semivida abaixo dos 5 minutos. Esta cinética complica os estudos de interação dado que se torna difícil de distinguir a ação do complexo da dos seus produtos de decomposição.

As nanopartículas de ouro (AuNPs) apresentam vantagens como sistemas de *drug delivery* dada a biocompatibilidade e facilidade de combinação com biomoléculas. Por esse motivo, um nanoconjugado deste tipo (AuNP@PEG@BSA@CORM-3), com polietilenoglicol (PEG), BSA e CORM-3, foi desenvolvido no laboratório onde o presente trabalho se inclui, apresentando maior eficiência anti-inflamatória em monócitos humanos quando comparado com o complexo metálico livre. A diferente internalização celular do CORM-3 quando livre e combinado surge como possível explicação para a diferença de eficácias anti-inflamatórias. Neste trabalho, tal hipótese é estudada por Espectrometria de Emissão Atómica por Plasma Acoplado Indutivamente de modo a quantificar o Ru e o Au nas células. Embora os resultados apontem para possíveis problemas na preparação das amostras celulares, indicam uma internalização de nanoconjugado baixa e incompatível com a sugestão levantada.

Finalmente, a possibilidade deste sistema ser usado no tratamento da Artrite Reumatoide, uma doença inflamatória, foi explorada usando BSA para transporte de CORM-3 como ensaio preliminar aos nanoconjugados, em ratos com Artrite Induzida por Adjuvante (AIA). A falta de efeitos descritos para a dose de CORM-3 possível de vetorizar (0.0037 mg Kg^{-1}), sugere que este sistema não é viável no tratamento de inflamações sistémicas.

Termos-chave: monóxido de carbono, CORM-3, albumina, nanopartículas de ouro, nanoconjugado, artrite reumatoide

ABSTRACT

CO-Releasing Molecules (CORMs) are a novel class of pharmaceutical agents able to release carbon monoxide (CO) to cells and tissues in a controlled manner, thus mimic the previously seen homeostatic properties of gaseous CO, namely in inflammatory processes, with neglectable toxicity. CO-Releasing Molecule 3 (CORM-3) is a ruthenium (Ru) carbonyl metal complex known to release one of its CO ligands when in contact with proteins, which have been used to describe metal-CORMs different roles and properties both *in vitro* as *in vivo*.

Albumin is a key protein transporter of drugs in the bloodstream, therefore responsible for their pharmacokinetic profiles and ultimately efficiency. In the present work, UV-Vis analysis and fluorescent methods are used to study Bovine Serum Albumin (BSA) and CORM-3 interaction, showing little conformational changes upon CORM-3 incubation and an effective quenching described by the Stern-Volmer relationship. CORM-3 decomposition in the working phosphate buffer is also followed by UV-Vis spectroscopy showing a degradation rate constant of 0.0026 s^{-1} and a half-life of less than 5 minutes. This instability in water complicates interaction studies, since it becomes difficult to distinguish between the metal complex true action from its decomposition products'.

Gold nanoparticles (AuNPs) are suitable drug delivery systems due to their good biocompatibility and ability to be conjugated with biomolecules. Therefore, a nanoconjugate of this kind (AuNP@PEG@BSA@CORM-3), featuring polyethylene glycol (PEG), BSA and CORM-3, was developed by the same group were the present work is included, showing better anti-inflammatory efficiency in human monocytes than CORM-3 by itself. Given the fact that one nanoconjugate can load hundreds of metal complexes, cellular uptake could be the reason behind their different efficiencies. Herein, such hypothesis is studied using Inductively Coupled Plasma-Atomic Emission Spectroscopy (ICP-AES) as a way to quantify Ru and Au within cells. Although the collected data show possible sample preparation problems in the cell matrixes, the overall results point towards a much lower nanoconjugate uptake when compared to the free form of CORM-3, which seems incompatible with the suggestion previously made.

Finally, the possibility of such nanoconjugate to be used therapeutically against Rheumatoid Arthritis, a chronic inflammatory disease, is explored using BSA as a carrier, as a preliminary assay for the nanoformulation, in Adjuvant-Induced Arthritic (AIA) rats. The lack of effect at a 0.0037 mg Kg^{-1} of CORM-3's dose, rejects beforehand the possibility of this kind of system to be used against systemic inflammations.

Keywords: carbon monoxide, CORM-3, albumin, gold nanoparticles, nanoconjugate, rheumatoid arthritis

SYMBOLS AND NOTATION

$^{-/-}$	Zero Copies of the Gene
A	Pre-exponential Factor (in Arrhenius eq.)
Abs	Absorbance
AIA	Adjuvant-Induced Arthritis
AP	Activator Protein
AuNPs	Gold Nanoparticles
BSA	Bovine Serum Albumin
BVR	Biliverdin Reductase
CCR	Complete Culture medium Recipe
cGMP	Cyclic Guanosine 3',5'-Monophosphate
CIA	Collagen-Induced Arthritis
COHb	Carboxyhemoglobin
COP-1	CO fluorescent Probe 1
CORM-2	CO-Releasing Molecule 2
CORM-3	CO-Releasing Molecule 3
CORMs	CO Releasing Molecules
COX	Cyclooxygenase
CTs	Charge Transfers
Cys	Amino Acid Cysteine
DLS	Dynamic Light Scattering
DMARD	Disease Modifying Anti Rheumatic Drug
DTNB	5,5'-Dithiobis(2-nitrobenzoic acid) or Ellman's reagent
E_a	Activation Energy (in Arrhenius eq.)
EDC	*N*-(3-Dimethylaminopropyl)-*N*'-ethylcarbodiimide
F	Fluorescence Intensity
F_0	Fluorescence Intensity in Absence of Quencher
FBS	Fetal Bovine Serum
FSL	Fibroblast-Like Synoviocytes
HEWL	Hen Egg-White Lysozyme
HIFα	Hypoxia Inducible Factor alpha
HO	Heme Oxygenase
HOMO	Highest Occupied Molecular Orbital
HSA	Human Serum Albumin
HSP32	Heat Shock Protein 32
HUVECs	Human Umbilical Vein Endothelial Cells

$h\nu$	Photon's energy
ICAM	Intercellular Adhesion Molecule
iCORM-3	Inactive CO Releasing Molecule 3
ICP-AES	Inductively Couples Plasma – Atomic Emission Spectroscopy
IL	Interleukin
IFN-γ	Interferon gamma
iNOS	Inducible Nitric Oxide Synthase
JNK	c-Jun N-terminal Kinase
k	Degradation Rate Constant
K	General Rate Constant (in Arrhenius eq.)
k_q	Rate Constant of Fluorophore Accessibility
K	General Stern-Volmer Constant
K_D	Stern-Volmer Constant in a Dynamic Quenching
K_{ST}	Stern-Volmer Constant in a Static Quenching
LOD	Limit of Detection
LPS	Lipopolysaccharides
LSP	Localized Surface Plasmon
LSPR	Localized Surface Plasmon Resonance
LUMO	Lowest Unoccupied Molecular Orbital
MAPK	Mitogen-Activated Protein Kinase
Mb-CO	Carboxy-Myoglobin
MES	2-(N-morpholino)ethanesulfonic Acid
MW	Molar Weight
NADPH	Nicotinamide Adenine Dinucleotide
NF-κB	Nuclear Factor κB
NO	Nitric Oxide
NOS	Nitric Oxide Synthase
NPAS	Neuronal PAS Domain
NSAID	Nonsteroidal Anti-Inflammatory Drug
P	p-value
PAMPs	Pathogen-Associated Molecular Patterns
PBS	Phosphate Buffer Solution
PEG	Polyethylene Glycol
PI	Polydispersity Index
PMN	Polymorphonuclear Neutrophil
PPARγ	Peroxisome Proliferator Activator Receptor gamma
Q	Quencher

R	Ideal Gas Constant
RA	Rheumatoid Arthritis
RPMI	Roswell Park Memorial Institute
RT	Room Temperature
SD	Standard Deviation
SDS	Sodium Dodecyl Sulphate
SEM	Standard Error of the Mean
sGC	Soluble Guanylate Cyclase
STAT	Signal Transducer and Activator of Transcription
Sulfo-NHS	*N*-hydroxysulfosuccinimide
$t_{1/2}$	Half-life Time
THP-1	Human Acute Monocytic Leukaemia Cell Line
TLR	Toll-like Receptors
TNFα	Tumor Necrosis Factor alpha
UV	Ultraviolet
VCAM	Vascular Cell Adhesion Molecule
Vis	Visible
v/v	Volume per Volume
WGSR	Water-Gas Shift Reaction
w/v	Weight per Volume
ε	Molar Extinction Coefficient
$\lambda_{exc.}$	Excitation Wavelength
τ_0	Lifetime of the Fluorophore
ΔG^0	Change in Free Energy (Gibbs energy) (in Van't Hoff eq.)
ΔH^0	Change in Enthalpy (in Van't Hoff eq.)
ΔS^0	Change in Entropy (in Van't Hoff eq.)

TABLE OF CONTENTS

FIGURE INDEX

TABLE INDEX

I. INTRODUCTION

1. Carbon Monoxide (CO)

Carbon monoxide is a colorless, tasteless and odorless gas formed upon combustion of carbon compounds when in a restrictive supply of molecular oxygen (O_2) (Housecroft & Sharpe 2005, p. 366). It is generally recognized by its toxicity when inhaled or in contact with organs, often with lethal consequences (Thom *et al*. 2006, Rose *et al*. 2016).

These effects arise from the molecule's ability to bind to metals present in metalloproteins (Boczkowski *et al*. 2006). The most well-known example is the binding to Fe^{II} of hemoglobin (Hb), for which CO has an even higher affinity than O_2 itself. This CO complexation and the subsequent formation of carboxyhemoglobin (COHb) severely impairs the protein ability to release O_2 to the tissues due to allosteric changes in the tetramer (Rose *et al*. 2016). Although many assume that high blood levels of COHb alone are the cause of CO lethal and non-lethal toxicity, Goldbaum *et al.* dismissed this belief in an *in vivo* study with dogs (Orellano *et al*. 1976). Other studies indicate that its combined effects by inhibition of cytochrome *c* oxidase on mitochondria, free-radical generation and activation of the immune response are what contributes to the effects (Chance *et al.* 1970, Cooper *et al*. 2008, Rose *et al*. 2016).

Despite its bad reputation, in 1949 Sjöstrand established CO as an endogenous molecule by measuring its levels in the air exhaled by human subjects. Only in the late 60s, and in agreement with Sjöstrand observations of increased CO levels in conditions of abnormal blood cells degradation, it was found it to be a product of the Heme Oxygenase (HO) catalytic activity, which is the rate-limiting enzyme in the heme degradation pathway (Sjöstrand 1949, Tenhunen *et al*. 1968, Tenhunen *et al*. 1970).

1.1. Heme Degradation Pathway

Heme is a coordination complex comprising an Fe ion coordinated to a tetrapyrrole ring (*e.g*. heme *b*, figure I.1). The ability to change its oxidation state according to the protein environment makes it an adaptable biological catalyst, present as a prosthetic group in several essential proteins in aerobic organisms (Bowman *et al*. 2008, Dutra *et al*. 2014).

Regardless of its vital roles, free heme increases oxidative stress leading to cytotoxicity issues presumably via free radicals' formation, thus highlighting the importance of this pathway (Larsen *et al*. 2012).

This enzymatic mechanism was first elucidated in 1969 by Tenhunen and his team. They observed the requirement for Nicotinamide Adenine Dinucleotide Phosphate (NADPH) and O_2 in the process, implying the action of cytochrome P450 reductase as the electron donor for HO to convert free heme into equimolar amounts of biliverdin, CO and Fe^{II}

(Tenhunen *et al.* 1969). Later on, the heme degradation pathway was established as represented in figure I.1. (Tenhunen *et al*. 1970, Larsen *et al*. 2012, Otterbein *et al*. 2016).

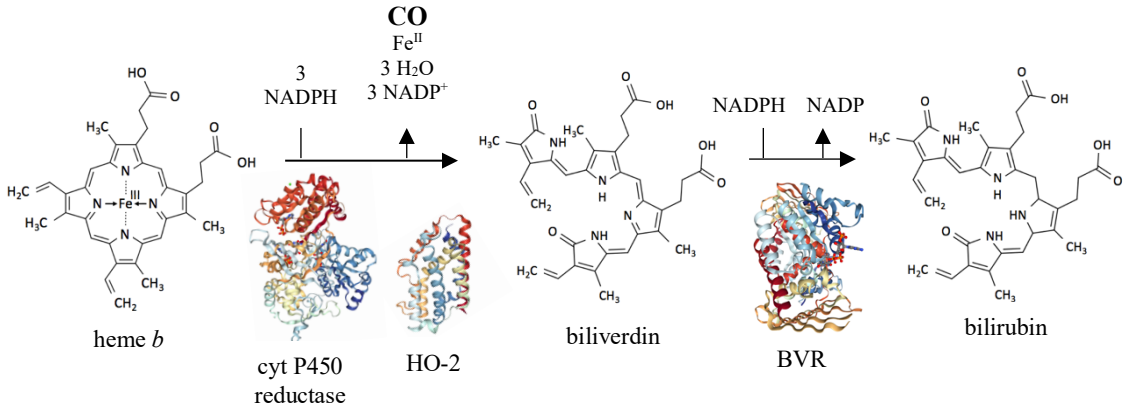

Figure I.1. Heme degradation pathway adapted from Spencer *et al.* (2014). HO cleaves the free heme at the α-methene bridge, with the carbon atom then released as CO. Cytochrome P450 reductase is necessary to the HO activity as it provides the electrons from NADPH. In mammals, biliverdin is later converted to bilirubin by the cytosolic enzyme Biliverdin Reductase (BVR). (PDB IDs: 3QE2, cyt P450 reductase; 5UC8, HO-2; 2H63, BVR)

There are two major isoforms of HO in mammals with catalytic activity, but different regulatory mechanisms: HO-1 is inducible and ubiquitously expressed, also called stress protein HSP32; whereas HO-2 is constitutive, mostly found in the brain and testes (Maines *et al*. 1986, Yachie *et al*. 1999).

1.1.1. Heme Oxygenase 1 (HO-1)

The upregulation of HO-1 occurs as a response to various stimuli such as hypoxia, inflammation, radiation, metal and pathogenic exposures, thus explaining why HO-1 is considered to be one of the most trustworthy indicators of oxidative stress in cells. (Vile *et al*. 1994, Poss *et al*. 1997, Maines 1997, Mann *et al*. 2007, Wegiel *et al*. 2013).

Additionally, HO-1$^{-/-}$ mice (Poss *et al*. 1997, Kapturczak *et al*. 2004), and one human case (Yachie *et al*. 1999), displayed high and non-specific inflammatory changes, such as leukocytosis, hepatomegaly and lymph node swelling, as well as iron deposition.

Altogether, these data imply an important role for HO-1 in mammalian iron homeostasis, regulation of immune response and protection against oxidative damage (Kapturczak *et al*. 2004, Lin *et al*. 2007). The precise mechanism by which HO-1 exerts its protective effects it's not fully understood. Even so, there are evidences suggesting its products play a fundamental role, namely CO. (Poss *et al*. 1997, Poss *et al*. 1997b, Zhang *et al*. 2014, Otterbein *et al*. 2016)

1.2. CO as an Endogenous Regulator

The first sign that CO was a neurotransmitter (Verma *et al*. 1993) led to an increase in research about possible endogenous regulatory functions alike nitric oxide (NO), another gasotransmitter with therapeutic potential formerly recognized.

In fact, and similar to NO, CO is considered to be an endogenous vasorelaxant with cardioprotective properties, partly by upregulating the production of cyclic guanosine 3', 5' – monophosphate (cGMP), a key regulator of vessel tone and neural transmission in the brain (Morita *et al*. 1995, Wang *et al*. 1997, Ling *et al*. 2017).

Beyond that, exogenous and endogenous CO were shown to prevent apoptosis, both the extrinsic and intrinsic pathways. HO-1/CO has a protector effect against the cytokine Tumor Necrosis Factor α (TNFα)-mediated apoptosis, dependent on the activation of the transcription factor Nuclear Factor κB (NF-κB), together with activation of p38 Mitogen-Activated Protein Kinase (MAPK) (Brouard *et al*. 2002), and inhibition of caspase 8 pathway (Kim *et al*. 2006). Once again, both in rat primary pulmonary artery endothelial cells exposed to anoxia-reoxygenation (Zhang *et al*. 2003) as in human hepatocytes exposed to TNFα (Tsui *et al*. 2005), CO showed similar effects through activation of p38 MAPK.

MAPKs are enzymes that connect receptors at the surface of the cell to vital regulatory targets inside, being p38 proteins and c-Jun N-terminal Kinase (JNK) signaling pathways part of this group (Johnson *et al*. 2007). The net of receptors responsible for their activation are numerous and complex, including pro-inflammatory cytokine receptors and Toll-like receptors (TLR). The later is responsible for recognizing Pathogen-Associated Molecular Patterns (PAMPs), as lipopolysaccharides (LPS) in bacterial cell wall (Jeffrey *et al.* 2007).

These enzymatic systems control several cellular mechanisms such as apoptosis, cell differentiation and production of inflammatory mediators by targeting transcription factors, just as NF-κB and Activator Protein-1 (AP-1). In this way, these MAPK pathways can regulate gene expression, namely the production of more cytokines, as illustrated in figure I.2 (Chang *et al*. 2001, Jeffrey *et al*. 2007).

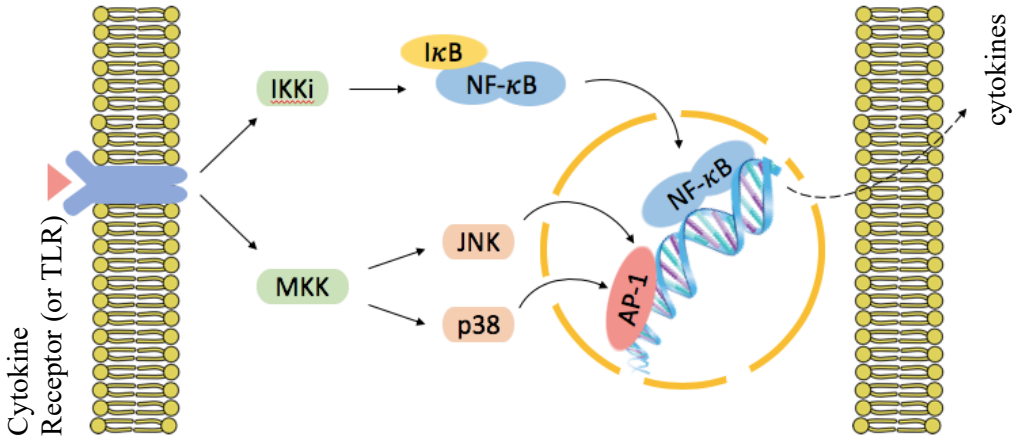

Figure I.2. Very simplified representation of the MAPK (JNK and p38 only) and NF-κB signaling pathways. MAPK are amplification cascades consisting of a three-kinase module: MAPK (not shown), MAPK Kinase (*e.g.* MKK) and MAPK Kinase Kinase (not shown). The complex IκB Kinase (IKK) mediates NF-κB translocation to the nucleus, via IκB degradation. JNK and p38 pathways can also modulate NF-κB activation dependent upon the stimuli (not shown) (Johnson *et al*. 2007, Jeffrey *et al*. 2007, Tornatore *et al*. 2012).

Cytokines are responsible for regulating and amplifying immune responses through several processes, namely by recruiting and activating leukocytes, promoting endothelial cell adhesion molecules expression, and increasing vascular permeability, among others, which ultimately leads to inflammation (Holdsworth *et al*. 2015).

Tuning into the scope of this work, of great interest are also the anti-inflammatory effects showed by CO, partly by acting on cytokine expression.

In a LPS-induced inflammation in macrophage, exogenous CO selectively inhibited the production of the pro-inflammatory cytokines Macrophage Inflammatory Protein-1β (MIP-1β), Interleukin-1 (IL-1β) and TNFα, while simultaneously increasing Interleukin-10 (IL-10), an anti-inflammatory one, through the p38 pathway and independently of cGMP, as confirmed by *in vivo* assays (Otterbein *et al*. 2000). In a mice model of sepsis, exogenous CO also decreased serum IL-1β and IL-6 levels. Further *in vitro* and *in vivo* studies suggested this effect to be linked to the JNK/AP-1 signaling pathway (Morse *et al*. 2003).

Other reports show similar results on suppressing pro-inflammatory cytokines (Hegazi *et al*. 2005, Chiang *et al*. 2013), including positive immunomodulatory effects after organ transplantation (Nakao *et al*. 2003, Nakao *et al*. 2005).

As already implied, CO does not act upon one single target (table I.1), but by interconnecting different signaling pathways (Wegiel *et al*. 2013).

Table I.1. Overall CO targets adapted from Wegiel *et al* (2013).

Hemeprotein	**Function**	**Primary location**
sGC	Vasodilatation	Vascular smooth muscle
Hemoglobin	CO delivery	Erythrocytes
NOS2	Nitric oxide generation	Leukocytes
NOS3	Nitric oxide generation	Endothelial cells
NPAS2	Transcriptional regulation	Neurons
Cytochrome oxidases	Bioenergetics	All cells
Non-hemeproteins	**Function**	**Primary location**
MAPKs	Signal transduction	All cells
PPAR$\boldsymbol{\gamma}$	Signal transduction	All cells
HIF$\boldsymbol{\alpha}$	Transcriptional regulation	All cells
STAT3	Signal transduction	All cells
NADPH oxidase	Free radical generation	Leukocytes

[1] sGC, soluble Guanylate Cyclase; NOS, Nitric Oxide Synthase; NPAS, Neuronal PAS Domain; PPARγ, Peroxisome Proliferator Activator Receptor γ; HIFα, Hypoxia Inducible Factor α; STAT3, Signal Transducer and Activator of Transcription.

Research on CO properties and mechanisms of action subsist today, making it the most comprehensively studied product of HO catalysis and the only one being translated into clinical use (Mann *et al*. 2007, Ling *et al*. 2017).

CO's inherent chemical stability and its restricted reactivity towards transient metals might make it a likely candidate for clinical applications (Romão *et al*. 2012). Even so, its low solubility in water and the potential harmful outcomes of a therapeutic centered on its gaseous form, both stand as key hindrances regarding its benefits (Ismailova *et al*. 2018).

CO-Releasing molecules (CORMs) arose as an answer on how to deliver therapeutic amounts of the molecule in a safe manner, by releasing CO upon certain triggers (Romão

et al. 2012). This discharge can be accomplished in different ways, as by a solvent-induced ligand exchange, a light stimulus (photo-CORMs), an enzyme (ET-CORMs) and less commonly, a change in pH, temperature or through an oxidation process (Ling *et al*. 2017). Additionally, contrary to inhaled CO, these molecules seem to be able to distribute CO to tissues with less formation of COHb (Bergstraesser *et al*. 2012).

2. Metal Based CORMs

Metal based CORMs are one of the most promising approaches due to the strong interactions between transition metals and CO. Moreover, the flexibility of molecular design by changing the CO neighboring ligands offers the possibility to tune its release, or even to target the complex (Schatzschneider 2015).

2.1. CO-Releasing Molecule 3 (CORM-3)

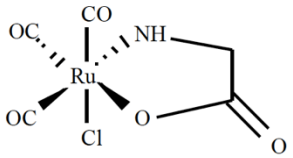

Figure I.3. Chemical structure of CORM-3, adapted from Motterlini *et al.* (2003).

Tricarbonylchloro(glycinato)ruthenium (II) (CORM-3) (figure I.3), with the chemical formula of [*fac*-Ru(k^2-$H_2NCH_2CO_2$)$(CO)_3$], is an example of a metal CORM, reported by Motterlini *et al.* to have therapeutic properties due to CO release when in a buffer solution, by a solvent-triggering process (Motterlini *et al.* 2003, Clark *et al*. 2003, Chaves-Ferreira *et al*. 2015). It is by far one of the most well studied and extensively characterized molecule of its kind, being continuously used to bring novel insides on CO effects both *in vitro* as *in vivo*.

The physicochemical properties of this complex rules its CO discharge and how it interacts with proteins, ultimately dictating its pharmacokinetic profile. Therefore, a brief description on these subjects is given below.

2.1.1. Physicochemical Properties

CORM-3 is a metal carbonyl complex soluble in water, in which the metal center is ruthenium (Ru) with an oxidation state of + 2, meaning an electronic configuration of [Kr]4d^6. According to the Molecular Orbital (MO) theory, the Highest Occupied Molecular Orbital (HOMO) of CO overlaps with the symmetrically adapted one of the metal, forming a σ-donor interaction. Even though usually this bond alone is not enough to hold the ligand to the metal, there is also a back-donation between the filled *d* orbitals of the metal and the vacant Lowest Unoccupied Molecular Orbital (LUMO) of CO (figure I.4). This synergic effect strengthens the interaction and is the reason behind the particular stability of carbonyl complexes of metals in the 6th and 10th group of the periodic table, like Ru itself. (Housecroft & Sharpe 2005, p. 44, Motterlini *et al*. 2003, Schatzschneider 2015)

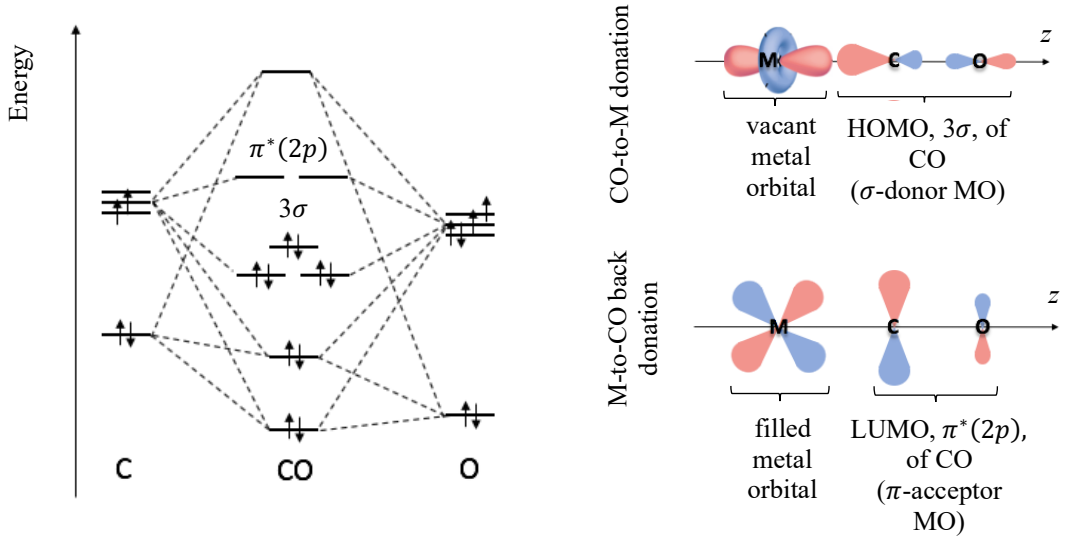

Figure I. 4. Qualitative molecular diagram of CO according to MO theory (left). Components of the Ru-CO bonding, assuming the z-axis as an example (right). Both representations are adapted from Housecroft & Sharpe (2005).

As previously stated, Motterlini *et al*. assessed the ability of CORM-3 to release CO in a 1:1 ratio, by measuring the formation of carboxy-myoglobin (Mb-CO) in the presence of deoxy-myoglobin, by the so-called *myoglobin assay* (Clark *et al*. 2003). Still, in a study using an amperometric CO sensor to directly measure CO release in phosphate buffer, pH 7.4, no CO was detected neither from CORM-3 nor CORM-2, which is another Ru-based CORM (Desmard *et al*. 2012). Later on, it was found that the sodium dithionite used to reduce all myoglobin prior to the myoglobin assay influences the CO release in a concentration-depended manner. At that point, evidences suggested the need of a complex environment, such as the intracellular milieu, for the release of CO by Ru-based CORMs (McLean *et al*. 2012).

Another study using Gas Chromatography-Thermal Conductivity Detection (GC-TCD) gave similar results with no CO detected when CORM-3 was dissolved in various aqueous solutions. Most importantly, it showed that CORM-3 binds covalently to proteins by histidine and aspartate residues, forming protein-$Ru^{II}(CO)_2$ adducts (figure I.5, A). This crystallographic evidence suggests that during the formation of such adducts, the non-CO ligands of CORM-3 are discarded, as well as one CO molecule. Nevertheless, no CO was directly detected, only Carbon Dioxide (CO_2) (Santos-Silva *et al*. 2011).

This CO_2 can be understood considering a Water-Gas Shift Reaction (WGSR) mechanism (Seixas *et al.* 2014, Chaves-Ferreira *et al*. 2015), where H_2 and CO_2 are produced from CO and H_2O. The precise mechanism by which ruthenium carbonyls catalyze this

reaction in not completely understood. Yet, there is consensus in the first step being an attack of a hydroxide (OH^-) to a CO ligand yielding a metallocarboxylic acid (M-COOH), followed by a second step of decarboxylation. In this way, the release of the CO ligand would be in the form of CO_2 (Chen *et al*. 2012, Schulz *et al*. 2013, Stepic *et al*. 2019). This was further confirmed by crystallographic evidences of a COOH ligand still bound to Ru in a Hen Egg-White Lysozyme (HEWL) adduct (Seixas *et al*. 2014).

In a study using a CO-selective fluorescent probe (COP-1), Chaves-Ferreira *et al.* observed an increase in fluorescence in phosphate buffer, pH 7.4, and in cells, both incubated with BSA-$Ru^{II}(CO)_2$ and HEWL-$Ru^{II}(CO)_2$ adducts. As previously proposed by Santos-Silva *et al*., this further hinted that the process of interaction with proteins is responsible for the CO release as in figure I.5 (B), and not CORM-3 by itself, a WGSR catalyst. Additional mass spectrometry measurements predicted an average of 7 modified His residues in Bovine Serum Albumin (BSA) upon binding.

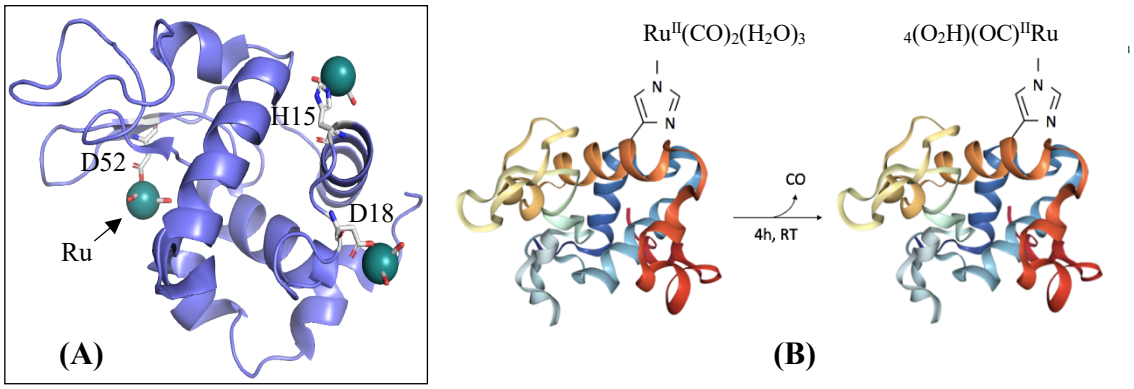

Figure I.5. Molecular models of protein-CORM interactions. **(A)** HEWL (in blue) residues (His^{15}, Asp^{18} and Asp^{52}, coloured by element) bound to three moieties of CORM-3 (coloured by element), prepared using PyMOL software, (PDB IDs: 6XJW, Santos-Silva *et al.* 2011). **(B)** CO release from HEWL-$Ru^{II}(CO)_2$ adducts, adapted from Chaves-Ferreira *et al.* (2015). The His^{15} residue accurate position in the tertiary structure was not considered in this illustration, (PDB IDs: 6HY4, HEWL).

Although there is still some controversy around CO release from Ru-based CORMs, these adducts results, along with all the evidences of CORM-3 mimicking CO properties, point that CO is released from this metal complex and able to exert biological activity within cells (Seixas *et al*. 2014, Chaves-Ferreira *et al*. 2015). Hence, a brief description on the anti-inflammatory effects showed by CORM-3 so far is given below.

2.1.2. Biological Activity

Sawle *et al.* showed that CORM-3 at 10 to 100 µM can attenuate LPS-induced inflammation. Using mice macrophages, it reduced TNFα production and nitrite levels in a concentration-depended manner, with no apparent effect on iNOS expression. Cell

viability was not affected, dismissing possible cytotoxic effects. However, by following changes in glutathione levels they found that cellular exposure to more than 50 μM of CORM-3 promotes some stress. (Sawle *et al*. 2005) Bani-Hani *et al.* got similar results using a model of thrombin and/or Interferon gamma (IFN-γ)-induced neuroinflammation in mice BV-2 microglia. Neither p38 nor JNK pathways seemed to be mediating this salutary effect. (Bani-Hani *et al*. 2006) In Collagen-Induced Arthritis (CIA) mice model of Rheumatoid Arthritis, Ferrándiz *et al*. showed that 5 and 10 mg Kg^{-1} of CORM-3 reduces the production of the proinflammatory cytokines IL-1β, TNFα, IL-6, IL-2 and IFN-γ while enhancing IL-4, an anti-inflammatory mediator. Another *in vivo* study using the 2,4,6-Trinitrobenzene Sulfonic Acid (TNBS)-induced colitis mice model, established the ability of 10 mg Kg^{-1} of CORM-3 to significantly reduce the inflammatory response by decreasing the mRNA levels of the pro-inflammatory cytokines IFN-γ, TNFα and IL-17A, in $CD4^+$ T cells (Ferrándiz *et al*. 2008, Fukuda *et al*. 2014).

During inflammation endothelial cells are stimulated by cytokines to express new cell-surface proteins, such as Intercellular Adhesion Molecule-1 (ICAM-1) and Vascular Cell Adhesion Molecule-1 (VCAM-1), capable to interact and arrest leukocytes, as represented in figure I.6 (Pober 2002, Ley *et al*. 2007).

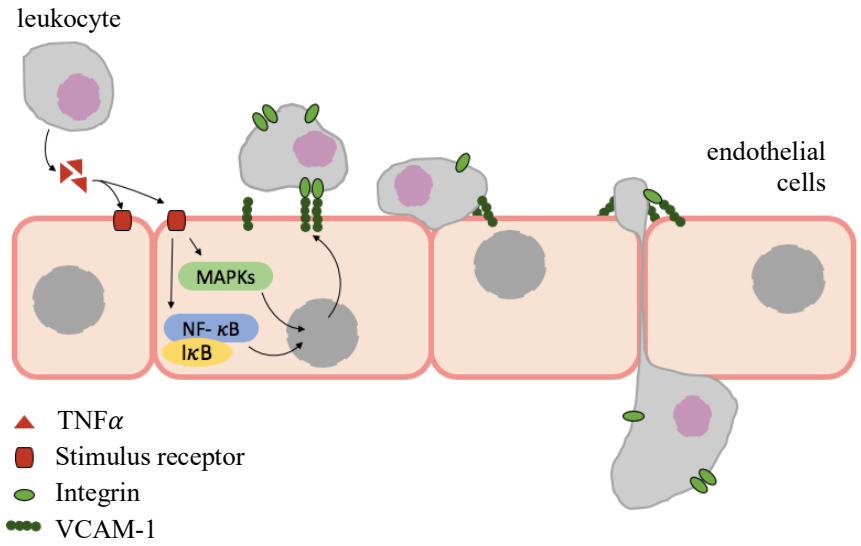

Figure I.6. VCAM-1-mediated leukocyte adhesion and migration across endothelial cells, adapted from Kong *et al*. (2018). Leukocytes secrete TNFα which up-regulates VCAM-1 in endothelial cells. This event promoted the accumulation of leukocytes at inflammation sites.

In two mice models of acute inflammation, CORM-3 successfully reduced the high numbers of peritoneal Polymorphonuclear Neutrophil (PMN) leukocytes by reducing their levels of adhesion molecules CD11b (an integrin) and L-selectin. Further *in vitro* studies using human cells, stablished PMN activation and migration upon the

endothelium as a likely target of CORM-3 anti-inflammatory effect *in vivo* (Urquhart *et al*. 2007).

Serizawa *et al.* assessed the ability of this metal complex to suppress the adhesion molecule VCAM-1 expression in human brain endothelial cells exposed to LPS, therefore inhibiting PMN adhesion through the JNK/AP-1 signaling pathway. In 2012, Bergstraesser *et al*. confirmed a loss of proadhesive phenotype in Human Umbilical Vein Endothelial Cells (HUVECs) exposed to TNFα, but due to p38 inhibition and/or damages in the mitochondrial respiratory chain (Bergstraesser *et al*. 2012, Serizawa *et al.* 2015).

All the above data suggest that CORM-3 further moderates the inflammatory response *in vivo* by reducing the interaction between leukocytes and endothelial cells (Ferrándiz *et al*. 2008).

Additionally, it is important to mention that the inactive form of CORM-3 (iCORM-3, *i.e.* CORM-3 left in solution for 24 h in order to lose its CO ligands) failed to reproduce the same results (Sawle *et al*. 2005, Ferrándiz *et al*. 2008, Serizawa *et al.* 2015). iCORM-3 arose in early studies in order to distinguish the biological effects of the metal structure itself (as well as degradation products) from CO's. However, such specie is not fully characterized and, in fact, iCORM-3 should be a mixture of water and CORM-3 products, still retaining a part of inert CO ligands (Seixas *et al*. 2013).

Finally, given the broad biological properties of CORMs, there are various diseases in which these molecules could play a therapeutic role (Ling *et al*. 2018), one of those being Rheumatoid Arthritis.

3. Rheumatoid Arthritis

Rheumatoid Arthritis (RA) is an autoimmune disease with unknown cause but with genetic susceptibility, affecting 1-2% of the worldwide population, with prevalence in woman (McInnes *et al*. 2011, Kumar *et al*. 2016).

This medical condition pathophysiology is uncertain and characterized by synovial inflammation and swelling on the joints, bone and cartilage degradation, as well as some systemic features such as pulmonary and cardiovascular complications (McInnes *et al*. 2011).

The synovial membrane (or synovium) is comprised of connective tissue covering joints cavities. The unrestrained infiltration of leukocytes in these tissues promotes the activation of osteoclasts cells and Fibroblast-Like Synoviocytes (FSL) in the joint. This phenomenon leads to swelling and bone destruction caused by the production of proteases by these cells, as well as extra tissue formation (pannus) by abnormal cell proliferation. (Townsend 2014)

The uncontrolled action of diverse inflammatory mediators contributes to RA pathogenesis as listed in table I.2.

Table I.2. Some mediators implicated in RA adapted from Kumar *et al.* (2016).

Mediator	Function
IL-1[2]	Initial modulator of inflammation
IL-2[2]	Inducer of inflammation
IL-6[2]	Stimulates B cells to produce autoantibodies
IL-15	Stimulates T cells proliferation
IL-16	Anergizes $CD4^+$ T cells
IL-17[2]	Increases the release of proinflammatory cytokines from macrophages
IL-18	Regulates IFN-γ
IFN-γ[2]	Facilitates pannus formation and promotes FLS
TNFα[2]	Inducer of inflammation
COX-2[2]	Converts arachidonate to PGH2, important for prostaglandins generation (mediators of inflammation)
CRP	Induces RANKL expression and modulates osteoclasts differentiation

[1] COX-2, Cyclooxygenase-2; PGH2, Prostaglandin H2; CRP, *C* Reactive Protein

[2] confirmed to be modulated through CO

The most common treatments for RA are synthetic drugs, only able to ameliorate pain and slow down symptom's progression. These include Nonsteroidal Anti-inflammatory drugs (NSAIDs) that inhibit cyclooxygenases (COXs) (*e.g*. Aspirin and Celecoxib), Disease Modifying Anti Rheumatic Drugs (DMARDs) that regulate cytokine action (*e.g.* Methotrexate), and Corticosteroids, also with immunoregulatory effects (*e.g*. Dexamethasone). However, frequent side-effects and lack of some patient's response urges the development of new strategies. (Kumar *et al*. 2016)

RA inflammatory signature makes this disease one of the most likely candidates for a CO-based therapy, as already assessed in different reports (Takagi *et al*. 2009, Maicas *et al*. 2010, Ibáñez *et al*. 2012).

In the past century some Au compounds were used to treat RA, *e.g.* Auranofin. However, and as mentioned before, their use was replaced by novel agents. Nonetheless, some believe there is still room for gold-based products in RA therapy, only this time in the form of nanoparticles (Faa *et al*. 2018).

4. Gold Nanoparticles in Medicine

Materials having between 1 to 100 nm are called nanomaterials. This nanoscale size is responsible for the distinctive physicochemical characteristics not seen in bulkier forms. (Lopez-Chaves *et al*. 2017)

AuNPs are probably the best example of these nanomaterials practical value in medicine, as for imaging, photothermal therapy, bio-sensing and drug-delivery purposes (Kong *et al*. 2017). This is partly due to their unique light-matter interaction properties, responsible for the red color seen in colloidal AuNPs (10 – 30 nm) (Chow *et al*. 1994). Their surface electrons (plasmon) oscillate collectively and confined in a narrow space, contrary to the bulk form (yellow), hence the so-called *Localized* Surface Plasmon (LSP). When a resonance condition is met, and the frequency of irradiated light matches the frequency of this plasmon, the absorption of light is maximum. This LSP is very sensitive and changes its resonance frequency upon changes in its environment, making interactions between AuNPs and biomolecules relatively easy to follow by spectrophotometric methods, as displayed in figure I.7. (Sperling *et al*. 2008, Panahi *et al*. 2017, Kong *et al*. 2017)

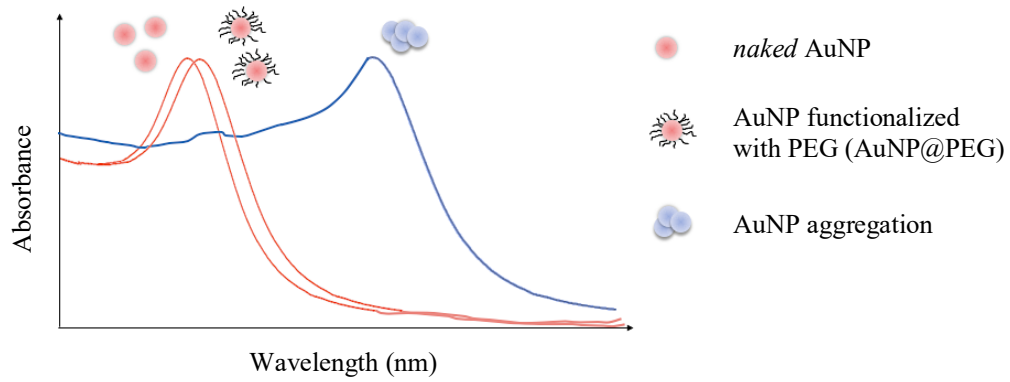

Figure I.7. Localized surface plasmon resonance peaks. AuNP SPR shift before (naked AuNP) and after functionalization with a biomolecule (AuNP@PEG). When AuNPs aggregate the shift is evident even at naked eye, as highlighted by the curve's different colour.

Due to a high surface-to-volume ratio and affinity towards thiol (-SH) and amine ($-NR_3$) groups, AuNPs can be functionalized with a large range of molecules, such as oligonucleotides, polyethylene glycol (PEG) and proteins (Raposo *et al*. 2007, Fernandes *et al.* 2017, Veigas *et al.* 2019) Moreover, AuNPs biocompatibility and ability to conjugate such elements in water phase reactions are major advantages regarding *in vivo* administration as well as targeting, making AuNPs suitable systems for drug delivery. (Porcaro *et al*. 2016, Fernandes *et al*. 2017, Lopez-Chaves *et al*. 2017). Therefore, a

vectorization of CORM-3 using gold nanoparticles could be a valuable strategy towards better efficiency.

II. OBJECTIVES

One way to improve the effect of pharmacological agents within tissues is to deliver them to the action sites. Considering all the anti-inflammatory effects of CORM-3 described in the introductory section, the development of novel nanoconjugates@CORM-3 using gold nanoparticles might enhance the effects of CORM-3. With this in mind, one of the most important aims of this work was to:

i) study CORM-3 interaction with albumin, BSA, in order to develop a nanoconjugate that includes both species - AuNP@PEG@BSA@CORM-3. UV-Vis spectroscopy and fluorescence quenching studies were used to assess conformational changes in the protein and to examine the magnitude and stability of the interaction BSA-CORM-3, after which the synthesis and characterization of AuNP@PEG@BSA@CORM-3 began.

During this work, such nanoconjugate showed improved anti-inflammatory effects *in vitro* when compared to free CORM-3 (Fernandes *et al*. 2020). To further understand the biological effects and therapeutic potential of AuNPs@PEG@BSA@CORM-3 compared to free CORM-3, additional *in vitro* and *in vivo* studies were needed. Consequently, two complementary goals were set:

ii) Inductively Coupled Plasma-Atomic Emission Spectroscopy (ICP-AES) analysis to compare the cellular uptake of CORM-3 when in the nanoconjugate and in the free form;

iii) *In vivo* assays in an Adjuvant-Induced Arthritis (AIA) rat model that mimics human Rheumatoid Arthritis.

III. MATERIALS AND METHODS

1. UV-Vis Spectroscopy

CORM-3 (Sigma-Aldrich) and BSA (Sigma-Aldrich) were dissolved in a 10 mM, pH 7, phosphate buffer solution containing 0.15 M NaCl. Seven samples of BSA at 8 μM and CORM-3 at 600, 400, 300, 200, 100, 50 and 25 μM, were prepared following a serial dilution, plus one left with BSA alone. BSA samples were prepared prior to CORM-3's preparation and addition, also dissolved in the same buffer. Absorbance measurements were performed at different incubation times (10 min, 1 h and 24 h), at room temperature.

A sample of CORM-3 at 400 μM was prepared in the same buffer and its absorbance was recorded several times during a period of three days.

All spectra were recorded in a range of 200 – 400 nm, on a UVmini-1240 UV-VIS Spectrophotometer (Shimadzu). Replicates were made for each sample.

2. Fluorescence Quenching

CORM-3 and BSA were dissolved in a 10 mM, pH 7, phosphate buffer solution containing 0.15 M NaCl. Seven samples of BSA at 2 μM and CORM-3 at 100, 50, 25, 12.5, 6.25, 3.125 and 1.5625 μM were prepared following a serial dilution, plus one left with BSA alone. Considering the decomposition of the metal complex, BSA samples were prepared prior to CORM-3's preparation and addition, also dissolved in the same buffer. Fluorescence measurements were performed at different incubation times (1 and 24 h) and different temperatures (298, 302, 306 and 310 K).

Emission spectra were recorded in a range of 300 – 425 nm upon excitation at 295 nm, on a Cary Eclipse Fluorescence Spectroscopy (Agilent). Replicates were made for each sample.

3. AuNP@PEG@BSA@CORM-3 Preparation

3.1. AuNP Synthesis

Standard AuNPs (15 nm) already synthetized in the laboratory (Nanomedicine lab., Departamento de Ciências da Vida – DCV, in FCT-UNL) were used to carry out functionalization. This colloidal solution was prepared using the citrate reduction method, described by Lee and Meisel (Lee *et al.* 1982), and characterized by UV-Vis spectroscopy, on a UVmini-1240 UV-VIS Spectrophotometer (Shimadzu), and by Dynamic Light Scattering (DLS), on a SZ-100 instrument (Horiba).

3.2. AuNP@PEG Functionalization

AuNPs were incubated overnight at 10 nM, with 0.028% (w/v) Sodium Dodecyl Sulphate (SDS) (Sigma) and a heterobifunctional PEG, HS-PEG(8)-COOH, (Iris Biotech) at 0.01 mg mL^{-1} in milli-Q H_2O, under agitation at room temperature.

After a 16 hours incubation period, the solution was centrifuged (Sigma 3-16K) at 14 000 *g* for 30 min at 4 °C and the supernatant stored in new eppendorfs in order to quantify the excess of PEG by the Ellman's assay. The pellet was then washed with milli-Q H_2O and centrifuged in the same conditions as before, thrice.

A solution of 5,5'-Dithiobis(2-nitrobenzoic acid) (DTNB) (Sigma) was prepared at 1.5 mg mL^{-1} and used as the Ellman's reagent. Ten solutions of the same PEG, at between 0.001 and 0.1 mg mL^{-1}, were prepared in order to do the calibration curve. The Ellman's assay was performed right after the washes using a 96-well plate, by adding the same amount of Ellman's reagent and sample per well. After 15 min the plate was read at 412 nm using a plate reader Infinite M200 (Tecan).

The AuNPs@PEG hydrodynamic diameter was characterized by DLS and the concentration accessed by UV-Vis spectroscopy, through by their SPR peak, with $\varepsilon = 2.33 \times 10^{-8}$ M^{-1} cm^{-1}.

3.3. AuNP@PEG@BSA Functionalization

The previously prepared AuNPs@PEG solution was incubated at 21 nM with 1.25 mg mL^{-1} of sulfo-NHS (Sigma-Aldrich) and 0.312 mg mL^{-1} of EDC (Sigma-Aldrich), in 10 mM 2-(N-morpholino)ethanesulfonic acid (MES) (Sigma), pH 6.0, for 30 minutes under agitation at room temperature. Later, the solution was centrifuged at 14 000 *g* for 30 min at 4 °C and the supernatant replaced to the original volume by 2.5 mM MES, pH 6.1. BSA (Sigma-Aldrich) was immediately added at 10 µg mL^{-1} and the resulting solution was left overnight under agitation at room temperature.

After a 16 hours incubation period, the solution was centrifuged at 14 000 *g* for 30 min at 4 °C and the supernatant stored in new eppendorfs in order to quantify the excess of BSA by the Coomassie Plus (Bradford) assay. The pellet was then washed with milli-Q H_2O and centrifuged in the same conditions as before, twice.

Ten solutions of BSA at between 20 and 4 µg mL^{-1}, were prepared in order to do the calibration curve. The Coomassie Plus (Bradford) assay (Sigma Aldrich) was performed right after the washes using a 96-well plate, by adding the same amount of Coomassie reagent and sample per well. After a 10 minutes period the plate was read at 595 nm.

The AuNPs@PEG@BSA hydrodynamic diameter was characterized by DLS and the concentration accessed by UV-Vis spectroscopy, through by their SPR peak, with $\varepsilon = 2.33 \times 10^{-8}$ M^{-1} cm^{-1}.

3.4. AuNP@PEG@BSA@CORM-3 Functionalization

The previously prepared AuNPs@PEG@BSA solution was incubated at 6 nM with 6 µM of CORM-3, for 10 minutes under agitation at room temperature. The solution was centrifuged at 12 000 *g* for 30 min at 4 °C and the pellet resuspended in autoclaved PBS.

The AuNPs@PEG@BSA@CORM-3 hydrodynamic diameter was characterized by DLS and the concentration accessed by UV-Vis spectroscopy, through by their SPR peak, with $\varepsilon = 2.33 \times 10^{-8}$ M^{-1} cm^{-1}.

3.5. DLS Analysis

The Dynamic Light Scattering analysis was performed at 25 °C with a scattering angle of 90°. Samples of AuNPs, AuNPs@PEG, AuNPs@PEG@BSA and AuNPs@PEG@BSA@CORM-3 were prepared in milli-Q H_2O with 1 nM concentration each. The hydrodynamic diameters were determined using the average results of 3 measures for each specie.

4. THP-1 Cell Culture

THP-1 human acute monocytic leukaemia cells were grown in Roswell Park Memorial Institute medium (RPMI) (Invitrogen) supplemented with 1 % (v/v) antibiotic/antimycotic solution (*Pen-Strep+antimycotic*: 10 000 units mL^{-1} of penicillin, 10 000 µg mL^{-1} of streptomycin and 25 µg mL^{-1} of Funizone® Antimycotic; Invitrogen) and 10 % (v/v) Fetal Bovine Serum (FBS) (Invitrogen), together called Complete Culture medium Recipe (CCR). Cells were kept at 37 °C in a 99 % humidified atmosphere of 5 % (v/v) CO_2 (CO_2 Incubator Leec, UK), in 75 cm^2 culture flasks.

4.1. Cell Count

A solution containing 50 µL of cellular suspension, 350 µL of CCR and 100 µL of 0.4 % (w/v) trypan blue (Sigma) was prepared and placed on a hemocytometer (Hirschmann). The viable cells were measured using an inverted microscope. Only non-colored cells are considered viable. After cell counting, cell density was determined as in Equation III.1:

$$(III.1)\quad N_{viable\ cells}/mL = \frac{N_{viable\ cells} \times Dilution\ factor \times 10^4}{n},$$

with n being the number of squares in the hemocytometer used to quantify the viable cells ($N_{viable\ cells}$), and 10^4 the chambers volume in mm^3.

5. Evaluation of the Inflammatory Response *in vitro*

THP-1 cells were seeded at a concentration of 10^6 cells $well^{-1}$ in 6-well plates and exposed to 700 ng mL^{-1} of lipopolysaccharide (LPS, Sigma) for 2 h. After that period, 0.25 μM of free CORM-3 (and inactive form – iCORM-3) or 1 nM of AuNPs@PEG@BSA@CORM-3 (loaded with 0.25 μM of both active and inactive forms of CORM-3) were added for 3 h. Afterwards, the cells were harvested, centrifuged for 5 min at 200 *g*, at room temperature, and the total RNA extracted from cells pellets using TRIsure (Bioline) according to the manufacturer's instructions.

The total RNA (100 ng) was reverse transcribed using the NZY M-MuLV First-Strand cDNA Synthesis kit (Nzytech). The expression of the inflammation-related genes TNF-α and IL-6, as well as the housekeeping gene RNA18S, was determined by RT-qPCR, performed on a Corbett Rotor-Gene 6000 thermal cycler (Qiagen), using HOT FIREPol EvaGreen qPCR Mix according to the manufacturer's instructions (Solis BioDyne). RT-qPCR conditions were: an initial denaturation at 95 ºC for 15 min followed by 10 cycles of denaturation at 95 ºC (20 seconds), annealing at 50 ºC (20 seconds) and extension at 72 ºC (20 seconds), and an additional 20 cycles of denaturation at 95 ºC (20 seconds), annealing at 53 ºC (20 seconds) and extension at 72 ºC (20 seconds). The following primer sequences were used:

RNA18S:

Fwd, 5'-GTAACCCGTTGAACCCCATT-3'

Rev, 5'-CCATCCAATCGGTAGTAGCG-3'

TNF-α:

Fwd, 5'-CCAGGCAGTCAGATCATCTTCTC-3'

Rev, 5'-TATCTCTCAGCTCCACGCCA-3'

IL-6:

Fwd, 5'-GGTACATCCTCGACGGCATCT-3'

Rev, 5'-TCTTTGCTGCTTTCACACAT-3'

This experimental procedure was performed by Rita Mendes (Fernandes *et al*. 2020).

6. ICP-AES Experimental Assays

THP-1 cells were placed in 25 cm^2 culture flasks in CCR, at a cell density of $5x10^5$ cells mL^{-1}. Cells were then incubated with CORM-3 at both 2 μM and 5 μM for 1, 3 and 6 hours each, as well as AuNP@PEG@BSA@CORM-3 at 8 nM, as in table III.1.

Table III.1. ICP-AES sample preparation.

	AuNP@PEG@BSA@CORM-3			**CORM-3**					
Concentration	8 nM			2 μM			5 μM		
Incubation time (hours)	1	3	6	1	3	6	1	3	6

Note. 5 flasks with THP-1 cells alone were also left in the incubator for 6h in order to do the calibration curve

Past the incubation times, cells were centrifuged for 5 min at 300 *g*, 15 °C. The pellet was then washed with 1 mL of PBS and centrifuged in the same conditions as before. Both supernatants were placed together and 1 mL of *aqua regia* was added separately to both supernatant and pellet samples.

The quantification of Ru was determined for both fractions of all the assays. Au was simultaneously determined for the AuNP@PEG@BSA@CORM-3 assays.

The ICP-AES quantification of Ru and Au was performed as a contracted service at Laboratório de Análises – Serviço de Espectroscopia de Emissão Atómica, FCT-UNL, Departamento de Química (DQ).

7. Animals and Experimental Procedure

Twenty 8-weeks old female Winstar AIA rats (± 200 g) were purchased from Charles River Laboratories International and kept under Specific Pathogen Free (SPF) conditions at Instituto de Medicina Molecular (iMM, Lisbon University). The inoculation with *Mycobacterium tuberculosis* was done by a subcutaneous injection in the animals' right paw, promoting a systemic inflammation. CORM-3 formulations prepared in PBS were injected intraperitoneally at a dose of 0.037 mg Kg^{-1} after 4 days of RA induction, using BSA as a carrier in a 1:5 ratio, respectively – named BSA@CORM-3 (treatment group, $N = 5$). Healthy ($N = 5$), non-treated arthritic (RA) ($N = 5$) and BSA@iCORM-3-injected ($N = 5$) rats were used as controls.

A larger BSA@CORM-3 formulation was freshly prepared each day in order to use the remaining as BSA@iCORM-3 in the following.

The body weight and inflammatory scores were measured throughout the time of treatment. The inflammatory scores were covered using a scale of 0 to 3 (0 – absence, 1 – erythema, 2 – erythema and swelling, 3 – deformities and functional damage), for each paw. The sum of each paw score defines the total inflammatory score per animal. Rats were sacrificed by CO_2 narcosis after 15 days of treatment. Blood, paws and bone samples were collected afterwards.

7.1. Histology

Left hind paw samples collected after sacrifice were immediately fixed in 10 % neutral buffered formalin solution and then decalcified in 10 % formic acid. Samples were later dehydrated, embedded in paraffin, serially sectioned and stained with hematoxylin and eosin for examination of structural changes as well as cellular infiltration. Histopathological evaluation was done in a blinded fashion as a contracted service at iMM, using the semi-quantitative scores: Sublining Layer infiltration score (0 – none to diffuse infiltration, 1 – lymphoid cell aggregate, 2 – lymphoid follicles and 3 – lymphoid follicles with germinal center formation); Lining Layer cell number score (0 – fewer than three layers, 1 – three to four layers, 2 – five to six layers and 3 – more than six layers), Bone Erosion score (0 – no erosions, 1 – minimal, 2 – mild, 3 – moderate and 4 – severe erosions), Cartilage Surface (0 – normal, 1 – irregular, 2 – clefts and 3 – clefts to bone), and Global Severity score (0 – no signs of inflammation, 1 – mild, 2 – moderate and 3 – severe inflammation).

7.2. Statistical Analysis

Statistical differences between two groups were estimated by the Mann-Whitney test and between more than two by the Kruskal-Wallis test, using GraphPad Prism. Differences were considered statistically significant for $P < .05$.

1. BSA and CORM-3 Interaction Studies

Albumin (MW of ± 67 KDa monomer) is the most abundant plasma protein in humans and the main carrier of metabolites, hormones and drugs in the bloodstream (Ghuman *et al*. 2005). The pharmacokinetics, and ultimately the effectiveness of a drug, depends on how it interacts with this protein, explaining the importance of binding studies between both in the process of drug development. (Hu *et al*. 2004, Koly *et al*. 2015, Suryawanshi *et al*. 2016)

While being one of the most evolutionary variable proteins, it has three structurally homologous domains, I, II and III, each further divided in subdomains A and B, as in figure IV.1, with distinctive binding properties and an uncommon pattern of 17 disulfide bridges, explaining its very high stability (Bujacz 2012, Sekula *et al*. 2013).

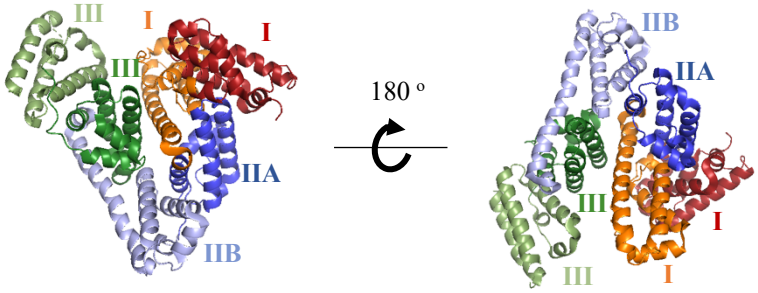

Figure IV.1. BSA domains and subdomains in different colors and shades, using PyMOL software (PDB ID: 3V03). The labelling was based on uniprot.org (entry P02769) and Majorek *et al.* (2012).

Human Serum Albumin (HSA) and BSA share more than a 75 % homology, both structural and sequential (see Appendix 1, *HSA and BSA Homology*). Because of such similarities, together with a high stability and easy accessibility, BSA is often used in affinity and kinetic studies instead of HSA (Bujacz 2012). These studies often include UV-Vis spectroscopy and fluorescence type of analysis (Xu *et al*. 2013), used in the present work in order to better characterize CORM-3's interactions with albumin.

1.1. UV-Vis Spectroscopy

1.1.1. CORM-3 Decomposition

The decomposition of CORM-3 in the working buffer was also followed by UV-Vis spectroscopy during three days (figure IV.2).

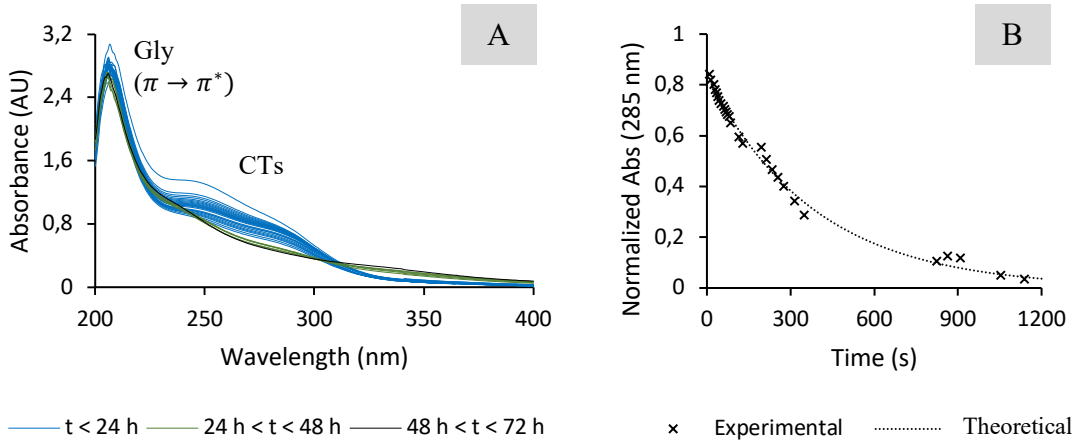

Figure IV.2. Decomposition of CORM-3 in the working buffer. (A) UV-Vis absorption spectra of CORM-3 at 400 µM recorded at different periods during 3 days. Gly, Glycinate; CTs, Charge Transfers. (B) Absorbance values at 285 nm over time.

The interpretation of metal complexes absorption spectra is not always straightfoward and can become very complex. Even so, some considerations can be made. The first and more intense band is here atributted to glycinate intra-ligand transitions ($\pi \rightarrow \pi^*$ character) (Bento *et al*. 1988, Pretsch *et al*. 2009, p. 47 and 48), not changing significantly over time. A pronounced decrease in absorbance between wavelengths of ± 250 – 295 nm becames apparent and stabilizes over time, with two bands clearly distinguishable – one more intense at ± 250 nm and a sholder at ± 290 nm. Other reports state a less intense and energetic band at such wavelenghts due to a charge transfer between Ru and the glycinate ligand (Yeh *et al*. 1980, Chagas *et al*. 2017), and between d^6 metals and carbonyl ligands (Gray *et al*. 1963). Therefore, the decrease in absorbance observed would be explained by the loss of those ligands.

In order to study this decomposition in more detail, the values recorded at 285 nm were normalized (see Appendix 1, *Data Normalization*) and plotted against time. The general equation IV.1 was used to describe the resulting exponential decay in figure IV.2, panel B.

$$\text{(IV.1)} \quad f(x) = f(0) \times e^{-kt},$$

where f (0) is the initial absorbance at 285 nm, k the degradation rate constant and t the time, in seconds (Schultz 1997, Groch 1998, Leike 2002). A non-linear fitting of this equation to the experimental data was done using the least square method with Solver in Excel, which provided equation IV.2, with $\sum X^2 = 0.013$.

$$\text{(IV.2)} \quad Abs_{285\ nm}(t) = 0.8385 \times e^{-0.0026\ t}$$

This degradation function is represented alonside the experimental values in figure IV.2, panel B.

This analysis allows to infer the degradation rate constant, k, of the CORM under study. According to the data obtained, $k = 0.0026\ s^{-1}$. This can be used to determine the half-life of the complex, $t_{1/2}$, using equation IV.3 (Groch 1998).

$$t_{1/2} = \frac{\ln(2)}{k} \quad \text{(IV.3)}$$

In this case, $t_{1/2} \cong 266$ s, meaning that half of CORM-3 in these conditions had decomposed after less than 5 minutes. This result is in agreement with Chaves-Ferreira *et al*., that accounted for a half-life of 3.6 min in human plasma due to CORM-3 instability in water. (Chaves-Ferreira *et al*. 2015).

Finally, no readings in the visible region were recorded in this assay. Although CORM-3 is colorless, it was noticeable a yellowish color developing over time. To confirm the results here obtained, further studies could be carried out were the decomposition of CORM-3 could be followed at this wavelength.

1.1.2. BSA Conformational Study

Absorption spectroscopy is also a simple and relevant method to explore conformational changes in proteins upon ligand binding (Hu *et al*. 2004, Suryawanshi *et al*. 2016). In order to assess possible conformational changes due to CORM-3 interaction, a fixed concentration of BSA (8µM) was incubated with different concentrations of CORM-3 (0 – 600 µM). Given this metal complex previously seen fast decomposition in the working buffer, spectra were recorded at different incubation times (figure IV.3).

As can be seen in black in figure IV.3, BSA has two absoption peaks. The protein backbone is responsible for the stronger peak at ± 220 nm, while the aromatic amino acid residues (Trp, Tyr, Phe) give rise to the weaker one at around 280 nm (Xu *et al*. 2013). Furthermore, disulfide bonds between Cys residues also absorb near 260 nm (Schmid 2001).

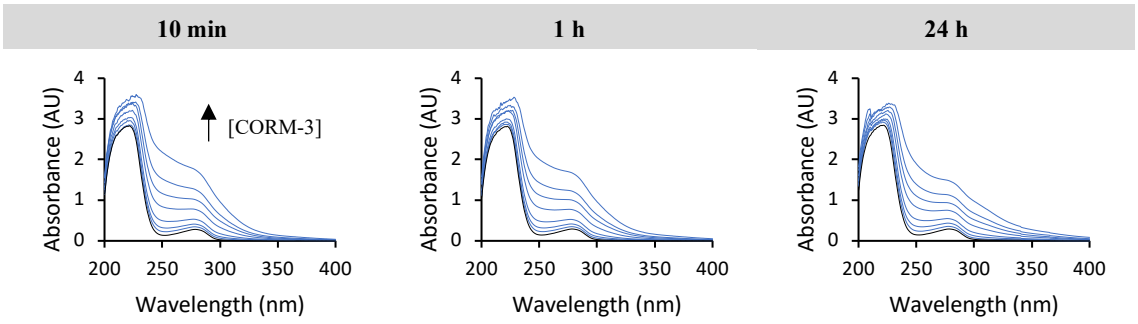

Figure IV.3. UV-Vis absorption spectra of free BSA (in black) and BSA with CORM-3 (in blue) after 10 min, 1 and 24 h incubations at room temperature and protein-to-ligand ratios varying from 1:3.125 to 1:75 (for spectral overlapp, see Appendix 3, *UV-Vis Interaction Analysis*). Black arrow highlights increasing concentrations of CORM-3 the higher the spectra.

It is known that at any wavelength the absorbance of a mixture is the sum of its components. Given the resemblances between BSA and CORM-3 absorption spectra, it's not possible to immediately grasp an interaction just by looking at the incubation spectra alone. With this in mind, both free BSA and CORM-3 spectra were arithmetically added and the comparison with the ones obtained for the BSA-CORM-3 incubation samples can be seen in figure IV.4, at diferent protein-to-ligand ratios.

In this thesis, only the 10 min comparison is shown, since both 1 and 24 h incubations showed identical results. Such similarity can be understood considering that: (i) after 10 minutes CORM-3 degradation is almost completed, as we have shown in section *1.1.1. CORM-3 Decomposition*, so the species in solution after that period should be highly similar; (i) the CORM-3 present in solution and subsequent decomposition products interact with BSA in similar ways, since nevertheless after 24 h it should be less CORM-3 present than at 10 min and the results were still identical (see Appendix 1, *UV-Vis Interaction Analysis*).

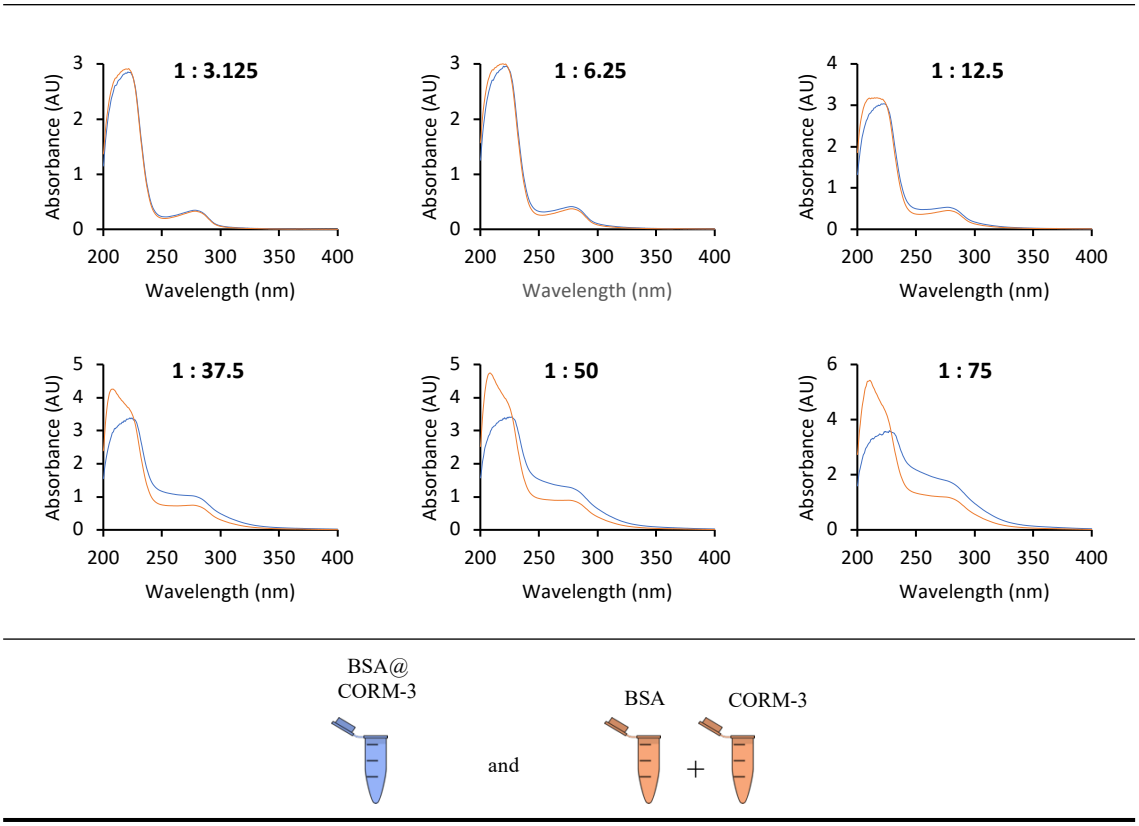

Figure IV.4. Comparison between spectra after 10 min incubation and the sum of free BSA and free CORM-3 resulting spectra, overlapped at different protein-to-ligand ratios.

As can be seen, the added spectra (in orange) do not overlap with the BSA-CORM-3 incubation spectra (in blue) and this becames even more evident the higher the CORM-3 concentration. A red-shift together with a decrease in absorbance appears around ± 230 nm with increasing concentration of ligand, as well as an increase in absorbance at the 250 - 300 nm range. This red-shift is consistent with an extend in the backbone of BSA upon CORM-3 incubation, which causes further exposure of the protein's hydrophobic regions. The increase in absorbance in the 250 - 300 nm range might suggest that CORM-3 can act as a denaturant at very high concentrations, since similar changes are consistent with unfolding by denaturants (Schmid 2001, Hu *et al*. 2004, Naik *et al.* 2013).

Finally, differences found in the lower 1 : 3.125 and 1 : 6.25 ratios are subtle so it is hard to tell if they are explained by CORM-3 action, even if apparently following the tendencies described for higher ratios.

To further understand the magnitude and stability of such interactions addditional studies are necessary using other techniques, such as fluorescence spectroscopy (Williams & Daviter 2013, p. 197).

1.2. BSA Fluorescence Quenching by CORM-3

Fluorescence is the emission of photons upon molecular relaxation from electronic excited states, typically associated with aromatic molecules (Lakowicz 2006, p. 1). Proteins containing Tyr, Phe and Trp residues, are fluorescent, with Trp as the main contributor due to a higher quantum yield and molar absorption coefficient, followed by Tyr and Phe (Williams & Daviter 2013, p. 174). BSA has two Trp (whereas HSA as only one - Trp^{214}) located in two distinct domains (I and II), which are represented in figure IV.5.

Figure IV.5. Model of BSA monomer highlighting the most important aromatic residues for the fluorescence signal, Trp^{134} and Trp^{212} (in black), and the most likely binding sites of CORM-3, His (blue spheres, left image) and Asp (red spheres, right image) residues. This image was prepared using PyMOL software (PDB ID: 3V03).

Trp^{212} is at the surface of the protein while Trp^{134} is in a hydrophobic cavity, known to be a binding site for many hydrophobic ligands (Li *et al*. 2011, Bujacz 2012, Jeremias *et al.* 2018). By setting the exciting wavelength at 295 nm, these two Trp residues become the only contributors to the fluorescence of a protein (Williams & Daviter 2013, p. 197).

This intrinsic fluorescence is often used as a way to study ligand interactions, namely through fluorescence quenching (Williams & Daviter 2013, p. 197). Any process that causes a decrease in fluorescence intensity can be considered as quenching. One example are molecular collisions between a fluorophore (*e.g.* Trp) and a molecule (*e.g.* CORM-3), named quencher (Lakowicz 2006, pp. 278 and 331). His^{18} and Asp^{450} are highlighted in figure IV.5 only because CORM-3 is known to bind strongly to these type of residues (Santos-Silva *et al*. 2011).

This type of quenching effect might be described by equation IV.4, known as the Stern-Volmer equation:

$$\text{(IV.4)} \quad \frac{F_0}{F} = 1 + \mathrm{K}\,[\mathrm{Q}],$$

where K stands for the Stern-Volmer constant, F_0 is the fluorescence intensity in the absence of quencher and F is the fluorescence intensity in the presence of a known concentration of quencher, [Q]. (Lakowicz 2006, p. 282, Williams & Daviter 2013, p. 172) Therefore, a similar method used in the UV-Vis analysis was used here to study BSA fluorescence quenching by CORM-3, where a fixed concentration of BSA (2 μM) was incubated with different concentrations of quencher (0 – 100 μM). Four different temperatures were used in order to understand the nature of the quenching effect, *i.e.* the stability of CORM-3 interaction.

Quenching data were plotted in figure IV.6 (see Appendix 1, *Intensity vs. Wavelength*).

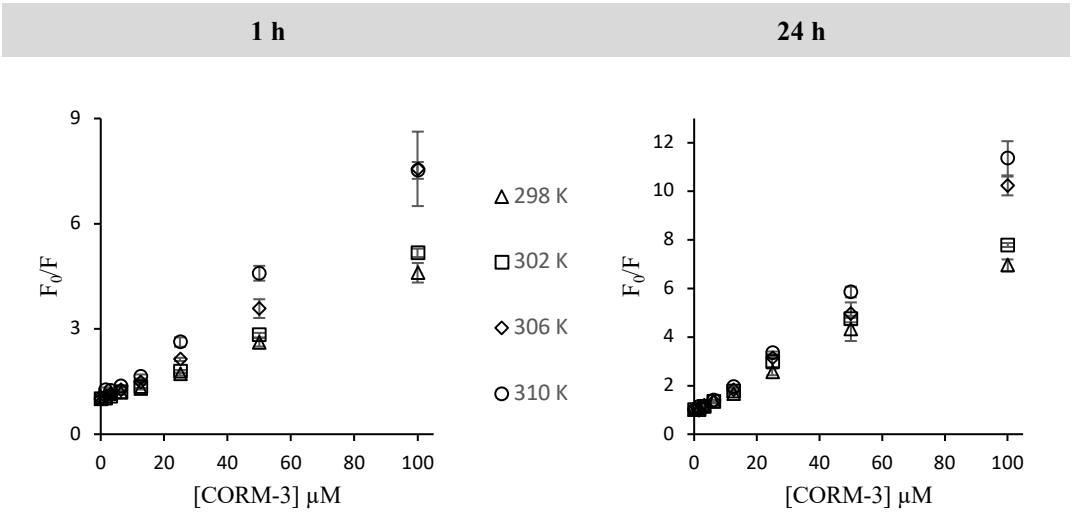

Figure IV.6. Stern-Volmer plots for BSA (2 μM) and CORM-3 (varying from 1.5625 to 100 μM) at different incubation times (1 and 24 h) and temperatures (298, 302, 306 and 310 K). Error bars correspond to SDs.

The slope of the regressions in figure IV.6 gives the Stern-Volmer constants, K_D, shown in table IV.1.

Table IV.1. Stern-Volmer constants taken from the slope of the linear regressions (and respective R^2).

time	T (K)	K_D (μM^{-1})	R^2
1 h	**298**	0.0356	0.994
	302	0.0416	0.995
	306	0.0647	0.987
	310	0.0660	0.996
24 h	**298**	0.0606	0.997
	302	0.0698	0.995
	306	0.0922	0.996
	310	0.1042	0.998

Good linear relationships between the fluorescence ratios and concentration of quencher were found within the chosen concentrations. Linear Stern-Volmer plots as the ones presented here, can be explained by only one of two processes: either a dynamic or a static quenching (Swadesh *et al*. 1987). Briefly, in a dynamic (or collisional) quenching the decrease in fluorescence is due to collisions between fluorophore and quencher, whereas in static is due to the formation of a stable non-fluorescent complex between both species, as illustrated in figure IV.7.

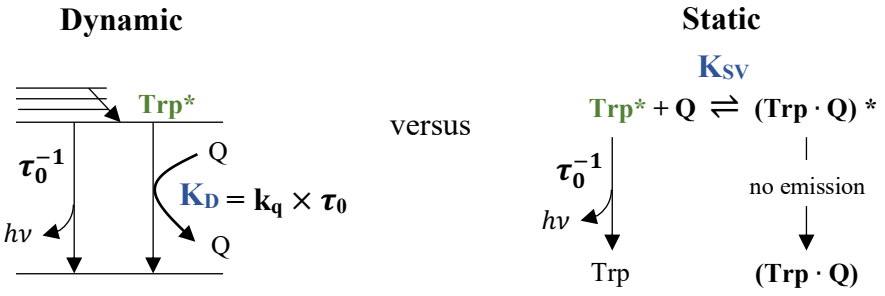

Figure IV.7. Comparison between dynamic and static quenching. A Jablonski diagram is used to illustrate the dynamic quenching with the horizontal lines representing the electronic states and vibrational modes of the fluorophore molecule. (Lakowicz 2006, pp. 11 and 280)

In the case of a **dynamic quenching** the Stern-Volmer constant ($\mathbf{K_D}$, in M^{-1}) is the product of a rate constant reflecting the fluorophore accessibility (k_q, in $M^{-1}s^{-1}$) and the lifetime of the fluorophore without quencher (τ_0, in s). In case of a **static quenching**, the Stern-Volmer constant ($\mathbf{K_{SV}}$, in M^{-1}) is an equilibrium constant for the complexation reaction (Lakowicz 2006, p. 281; Swadesh *et al*. 1987). Although mathematically the same, their physical meaning is entirely different, and this is empirically evident by their dependence on temperature.

In practice, in a dynamic quenching the K_D increases with increasing temperatures, whereas in a static quenching the K_{SV} decreases with increasing temperatures. (Swadesh *et al*. 1987). Based on the values from table IV.1, this immediately suggests that the quenching of BSA by CORM-3 could be a dynamic process.

However, in some cases of static quenching, higher Stern-Volmer constant values for increasing temperatures might arise from a positive change in entropy for the complex formation, $\Delta S^0 > 0$, as described by the Van't Hoff equation IV.5.

$$\text{(IV.5)} \quad \ln(K) = -\frac{\Delta H^0}{RT} + \frac{\Delta S^0}{R},$$

where K would be the equilibrium constant (K_{SV}), ΔH^0 and ΔS^0 the change in enthalpy and entropy, respectively, R the ideal gas constant and T the temperature. In this way, a deceptive K_D would in reality be a K_{SV}. This could happen in cases where hydrophobic interactions play an important role in the complex formation. (Swadesh *et al*. 1987)

Given Trp hydrophobic nature, if the constants in table IV.1 were actually due to static quenching (see Appendix 1, *ln K vs. 1/T*), this would also possibly explain why their magnitude is similar to some K_{SV} present in the literature (Lakowicz 2006, p. 282; Xu *et al*. 2013, Suryawanshi *et al*. 2016).

Another explanation for such high Stern-Volmer constants is CORM-3 decomposition itself. The release of the ancillary ligands, particularly glycinate, could make this a second quencher in solution. If so, because the real concentration of quencher would be systematically twice the used in these calculations (1:1, gly:CORM-3), it would result in larger F_0/F vs. [Q] slopes, *i.e.* K_D. In order to test such hypothesis further analysis in the presence of free gly should be carried out.

It might not be so straightforward to distinguish between dynamic or static quenching sometimes. Other analysis could be used to understand the type of process behind the effect, but only one would give definite results, which is to measure the fluorophore lifetime, since this wouldn't change in the presence of a static quencher. (Lakowicz 2006, p. 282) These studies should be carried out for the BSA-CORM-3 adduct.

In an attempt to improve the anti-inflammatory effects shown by free CORM-3 in other reports (Sawle *et al*. 2005, Ferrándiz *et al*. 2008, Fukuda *et al*. 2014), a pilot system of nanovectorized CORM-3 in gold nanoparticles (AuNP) using BSA was developed and studied in an *in vitro* model of inflammation by Rita Mendes, in the group where the present work is included (Fernandes *et al*. 2020).

2. Evaluation of the Inflammatory Response *in vitro*

AuNPs were synthetized by the Turkevich method (Turkevich 1985), which is the aqueous phase reduction of a gold salt ($HAuCl_4$) by sodium citrate ($Na_3C_6H_5O_7$), and then pegylated with a heterobifunctional PEG. BSA was later added through an amine coupling reaction, via the *N*-(3-Dimethylaminopropyl)-*N*'-ethylcarbodiimide (EDC) and *N*-hydroxysulfosuccinimide (NHS) activation of the PEG carboxylic group, represented in figure IV.8. The incubation of this arrangement with CORM-3 gave the final nanoconjugate, AuNP@PEG@BSA@CORM-3 (see Appendix 2, *Nanoconjugates Characterization*) (Fernandes *et al*. 2020).

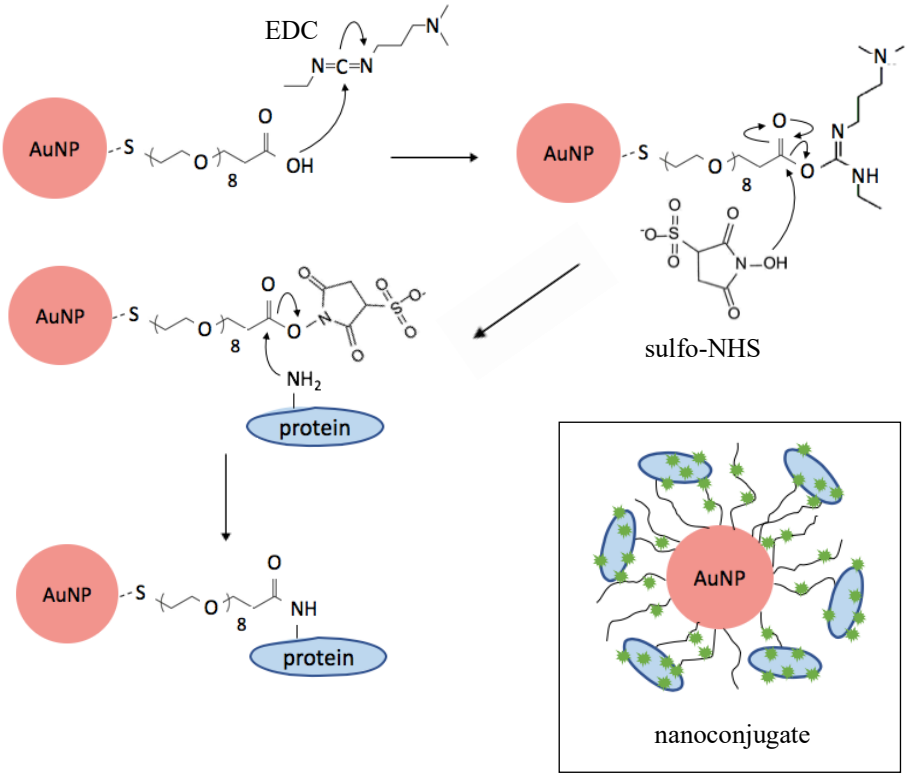

Figure IV.8. Two-step EDC/sulfo-NHS reaction mechanism. The carboxylic group (-COOH) in the modified PEG reacts with the sulfo-NHS in the presence of EDC, yielding a reactive ester towards primary amines ($-NH_2$) present in proteins. Sulfo-NHS is not crucial but enhances the reaction efficiency (Thermo Scientific, Instructions NHS and sulfo-NHS). Later incubation with CORM-3 (in green) yields the final nanoconjugate system, AuNP@PEG@BSA@CORM-3, with a predicted ratio of 1:1450:6:254 between species, respectively.

The anti-inflammatory effect of this nanosystem was assessed by evaluation of TNF-α and IL-6 gene expression in human monocytes exposed to LPS, as can be seen in figure IV.9 (Fernandes *et al*. 2020).

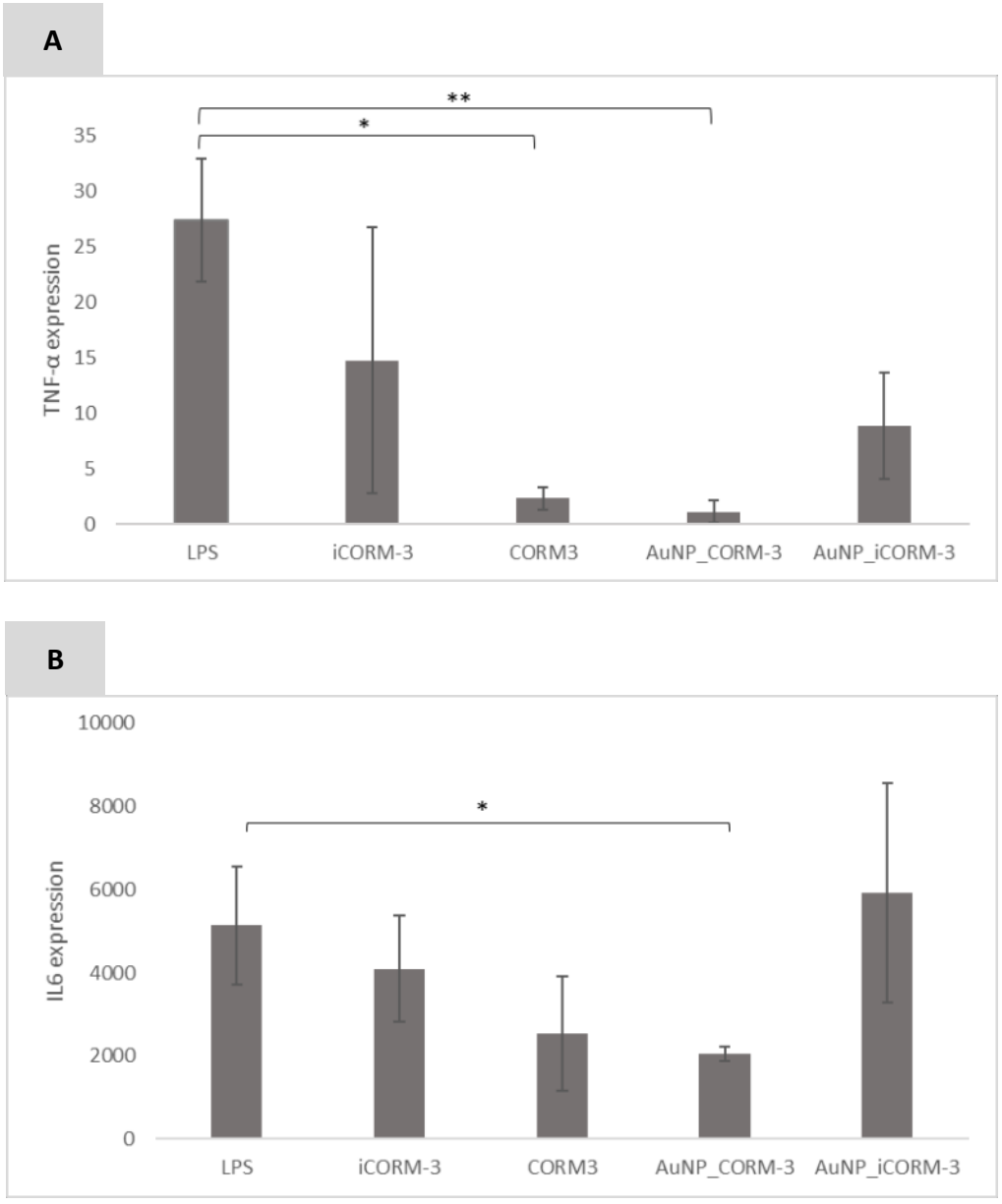

Figure IV. 9. Effects of free and functionalized CORM-3 (as well as the inactive form) onto AuNPs on (A) TNF-α and (B) IL-6 transcripts' expression levels in THP-1 cells after 2 h incubation with LPS, adapted from Fernandes *et al.* 2020. AuNP_CORM-3, AuNP@PEG@BSA@CORM-3; AuNP_iCORM-3, AuNP@PEG@BSA@iCORM-3. Data are expressed as means ± SEM (* $P \leq .05$, ** $P \leq .01$ compared to the control). These results were obtained by Rita Mendes.

Both free CORM-3 as AuNPs@PEG@BSA@CORM-3 significantly reduced the transcripts of TNFα and IL-6 pro-inflammatory cytokines in a way consistent with previous reports. More interesting, the nanoconjugate was better at decreasing these

mRNA levels, and with a lower SEM value when compared to CORM-3 alone. Since one nanoconjugate can load hundreds of metal complexes, differences in cellular uptake could explain the differences in the anti-inflammatory efficiencies found between these two forms of delivery.

3. Cellular Uptake

Inductively Coupled Plasma (ICP) is one of the best techniques to study nanoparticles internalization by cells due to its ability to detect within the range of ppt and ppm (Dykman *et al*. 2014, Matczuk *et al*. 2018). In this work, ICP coupled to Atomic Emission Spectroscopy (ICP-AES) was the method of choice for cellular uptake comparison between free CORM-3 and its vectorized form, AuNP@PEG@BSA@CORM-3. In this technique, the sample is introduced in a hot plasma that atomizes it to its elements, which are then determined and quantified based on their emission spectrum (Floyd *et al*. 1980).

THP-1 cells were incubated with both 2 µM and 5 µM of free CORM-3, and with 8 nM of nanoconjugate (see Appendix 2, *Nanoconjugates Characterization*), which loads 2 µM of CORM-3 (Fernandes *et al*. 2020), during 1, 3 and 6 hours. The results of the Ru and Au measurements after each incubation time, in cells (pellet) and media (supernatant), are presented in table IV.2.

Table IV.2. Quantification of Ru and Au by ICP-AES, both in cells (pellet) and media (supernatant), after cell incubation with free CORM-3 and AuNP@PEG@BSA@CORM-3.

Free [CORM-3]	**2 µM**			**5 µM**		
Element	**Ruthenium**					
Incubation time	**1 h**	**3 h**	**6 h**	**1 h**	**3 h**	**6 h**
Supernatant (mg/mL)	0.03	0.03	0,04	0.13	0.14	0.13
Pellet (mg/mL)	< LOD	< LOD	< LOD	< LOD	< LOD	< LOD

[AuNP@...@CORM-3]	**8 nM** (meaning 2 µM of CORM-3)					
Element	**Ruthenium**			**Gold**		
Incubation time	**1 h**	**3 h**	**6 h**	**1 h**	**3 h**	**6 h**
Supernatant (mg/mL)	0.11	0.11	0.12	72.3	69.8	77.2
Pellet (mg/mL)	0.016	0.021	< LOD	7.03	9.61	2.58

These data suggests that both CORM-3 as AuNP@PEG@BSA@CORM-3 internalization do not change significantly over time, which either means that (i) all the free CORM-3 and nanoconjugate were internalized in the first hour, or (ii) cells reached an equilibrium between internalization and excretion in the first incubation hour.

All Ru in free CORM-3 pellets was below the Limit of Detection (LOD), which suggests that a higher amount of Ru is internalized by cells when using AuNP@PEG@BSA@CORM-3.

It is important to remember that 8 nM of nanoconjugate takes 2 μM of CORM-3 (Fernandes *et al*. 2020). With this in mind, by looking at the supernatant values alone, the opposite seems true – that higher amount of Ru is internalized by cells when using free CORM-3, since more cellular uptake means less Ru in the supernatant.

These unclear results might be reflecting problems in sample preparation. Although AuNPs suspensions in cellular media (supernatant) are easier to digest and therefore quantify, the same does not happen in complex matrixes like cells. Usually, microwave digestion in closed pressured vials together with a strong acid is the best method to prepare such matrixes. Given such complexity, the subsequent analysis depends strongly on instrument calibration and can show a large scatter of data. (Dykman *et al*. 2014, Matczuk *et al.* 2018) Considering this, the present results might point towards problems in pellet preparation.

Nonetheless, what is not internalized by cells must be in the supernatant, which is a simpler matrix to handle. With this in mind, Ru in all pellets were determined by subtracting the supernatants from the initially CORM-3/nanoconjugate added. These results are displayed in tables IV.3 and IV.4.

Table IV.3. Ru determination in both fractions based on the supernatant values in table IV.2 and total CORM-3 added (2 µM × 5 mL flask volume × 10^{-3} = 0,01 µmol, and 5 µM × 5 mL flask volume × 10^{-3} = 0,025 µmol).

Free [CORM-3]	**2 µM**			**5 µM**		
Element	**Ruthenium**					
Incubation time	**1 h**	**3 h**	**6 h**	**1 h**	**3 h**	**6 h**
Supernatant (µmol)	1.78×10^{-3}	1.78×10^{-3}	$2{,}37\times10^{-3}$	7.72×10^{-3}	8.31×10^{-3}	7.72×10^{-3}
Pellet (µmol)	8.22×10^{-3}	8.22×10^{-3}	$7{,}63\times10^{-3}$	1.73×10^{-2}	1.67×10^{-2}	1.73×10^{-2}
Supernatant (%)	18	18	24	31	33	31
Pellet (%)	82	82	76	69	67	69

As can be observed, the uptake in the 2 µM assay was around 80 %, whereas in the 5 µM assay was slightly less, around 68 %, which might suggest a saturation of CORM-3 in cells.

AuNPs@PEG@BSA@CORM-3 analysis is trickier since it's not possible to determine the exact amount of gold nanoparticles solely based on gold concentration, but a theoretical approximation can be made: A 15 nm AuNP has a volume of $1.76625\text{x}10^{-18}$ mL (1766.25 nm^3). Considering the density of gold to be 19.30 g mL^{-1} (Reger *et al*. 1997, p. 935), in 1 nanoparticle is expected 3.40886×10^{-14} mg of Au. By dividing the detected quantity (mg) by this calculated value, we get the number of AuNPs in the supernatant, which further divided by the Avogadro's Number leads to the final amounts (nmol) in table IV.4.

Table IV.4. Ru (in µmol) and AuNP (in nmol) determination in both fractions based on the supernatant values given in table IV.2 and the total nanoconjugate added (8 nM × 5 mL × 10^{-3} = 0.04 nmol), for AuNP@PEG@BSA@CORM-3 assays.

[AuNP@...@CORM3]	**8 nM** (meaning 2 µM of CORM-3)					
Element	**Ruthenium**			**AuNP**		
Incubation time	**1 h**	**3 h**	**6 h**	**1 h**	**3 h**	**6 h**
Supernatant (µmol | nmol)	6.53×10^{-3}	6.53×10^{-3}	$7{,}12\times10^{-3}$	2.11×10^{-2}	2.04×10^{-2}	$2{,}26\times10^{-2}$
Pellet (µmol | nmol)	$3{,}47\times10^{-3}$	$3{,}47\times10^{-3}$	$2{,}88\times10^{-3}$	$1{,}89\times10^{-2}$	$1{,}96\times10^{-2}$	$1{,}74\times10^{-2}$
Supernatant (%)	65	65	71	53	51	56
Pellet (%)	35	35	29	47	49	44

Therefore, by dismissing pellet values, only around $3.30\times10^{-3} \pm 3.43\times10^{-4}$ µmol of Ru were internalized as nanoconjugate, which is less than the $8.0\times10^{-3} \pm 3.43\times10^{-4}$ µmol internalized as free CORM-3. Furthermore, the predicted Ru in cells, based solely on AuNPs in the supernatant, is around $4.7\times10^{-3} \pm 2.84\times10^{-4}$ µmol (means $\pm$ SD). This difference can be explained either by experimental fluctuations in CORM-3 loading, or by the fact that AuNPs determination was itself an approximation based on Au concentrations.

Although all pellet samples were dismissed as poorly digested, a table considering such results for AuNP@PEG@BSA@CORM-3 is still given in Appendix 2, *Considering Pellet Values*.

Less internalization of nanoconjugate when compared to CORM-3 is not totally unexpected. CORM-3 is a metal complex which should enter cells either by passive or facilitated diffusion (Puckett *et al*. 2008), whereas functionalized gold nanoparticles can only be internalized presumably via phagocytosis due to their large size (Dykman *et al*. 2014). Even so, one thing to be careful about with this type of studies is that, although cells were washed prior to sample preparation, it cannot be excluded the possibility of some Ru in the pellet be in fact Ru sequestered at the outer surface of the cell membrane. Nonetheless, these supernatant data suggesting such internalization amounts is not compatible with the cellular uptake explaining the nanoconjugate's higher efficiency.

Imaging technics could also be used to clarify this issue, namely Electron Microscopy (EM) and Synchroton-based X-ray Fluorescence (SXRF), or even Transmission Electron Microscopy (TEM) for AuNPs determination. However, each have their own

disadvantages, as for the complexity of sample preparation (again), low sensitivity and associated costs (Ralle *et al*. 2009, Matczuk *et al*. 2018). All in all, ICP-MS or ICP-AES remain the best option, so these assays should be repeated paying extra attention to cell matrixes preparation.

4. BSA@CORM-3 Adducts Against an *In Vivo* Model of RA

Rheumatoid Arthritis appeared as one of the best candidates to explore the therapeutic use of the gold-nanoconjugate AuNP@PEG@BSA@CORM-3 with the already assessed anti-inflammatory properties in cell-based assays (Fernandes *et al*. 2020). Based on previous reports about CORM-3 action *in vivo*, its preferential dose would be ranging from 5 to 10 mg Kg^{-1} day^{-1} (Ferrándiz *et al*. 2008, Maicas *et al*. 2010). Taking this into account and having in mind a maximum injection volume of 1 mL per rat, a dose of 10 mg Kg^{-1} would mean an AuNP@PEG@BSA@CORM-3 solution highly concentrated, > 25 000 nM. This is not a realistic option since AuNPs and nanoconjugates are susceptible to aggregate when in very concentrated solutions, posing a key limitation on CORM-3 dosage. Therefore, a theoretical limit of concentration was set at 100 nM, resulting in the lower 0.037 mg Kg^{-1} dose of CORM-3 (see Appendix 3, *Dose rationale*). Again, this set value is a theoretical one with no guarantees of a good reproducibility of no aggregation to endure a 15 days experiment.

As a way to overcome such issue, it could be suggested a higher volume of injection and/or more than one per day. However, (i) the invasive nature of the procedure itself would contribute to inflammation in either ways, (ii) for ethical reasons animal handling must be as little as possible and (iii) a therapy based on multiple daily injections would not be practical nor convenient for patients.

All values and costs considered, it was decided to run an experiment with a simpler BSA@CORM-3 system, at a dose of 0.037 mg Kg^{-1} of CORM-3, in order to evaluate the interest of an AuNP@PEG@BSA@CORM-3 approach beforehand.

There are various rodent models used to mimic RA in preclinical phases of drug development. A common example being the administration of exogenous elements to trigger the inflammatory process, as in Bacterial cell wall-induced arthritis, CIA and AIA.

AIA can begin through administration of three different materials: lipoidal amine, pristane and *Mycobacterium tuberculosis*. In spite of the superior inflammatory severity that characterizes the use of *Mycobacterium tuberculosis*, the lesions are more consistent among individuals and studies, making it preferential over the other two (Bolon *et al*. 2011). Despite the strong resemblances regarding joint inflammation and certain systemic features, no animal model completely mimics human RA (Joe *et al*. 1999).

In this study, AIA is the chosen animal model for two main reasons, (i) as mentioned, it's one of the most reliable models of RA in rats and (ii) TNFα is considered to be the "master" proinflammatory cytokine driving AIA immune response (Bolon *et al*. 2011), which is one of the main targets of AuNP@PEG@BSA@CORM-3 action (Fernandes *et al*. 2020).

In a study made by Stolina *et al*., this model's progression of RA was divided into pre-clinical, acute and chronic phases, showing how cytokine profiles change over time, both locally (sustained mainly by IL-1α, IL-1β, IL-6 and IL-17) and systemically (sustained mainly by TNFα, IL-17 and IL-18) (Stolina *et al*. 2009).

Formulations of BSA@CORM-3 were injected intraperitoneally and once a day, after 4 days of RA induction with *Mycobacterium tuberculosis*. The BSA@CORM-3 formulation was prepared each day immediately before animal's injection, assuring that the CO-Ru content was as high as possible. Part of this formulation was kept for the following day and used as a control - BSA@iCORM-3, were all CO moieties had theoretically already been released.

In the present work, the pre-clinical phase lasted until the 9th day of treatment (*i.e.* before onset of clinically visible arthritis) (figure IV.10, panel A), which corresponds to the 13th day after RA-induction. This time period is larger when compared to previous analyses reporting an end by the 5th day of treatment (Stolina *et al*. 2009, Bolon *et al*. 2011, Cascão *et al*. 2015, Vidal *et al*. 2015).

In some cases, individuals might fail to develop the disease due to either a leakage of *Mycobacterium* at the injection site or lack of uniformity in loading the syringe (Animal Models of Disease 2001). Since all RA-induced groups developed RA analogously, the hypotheses above are discharged.

According to the same authors, the clinical phase ends and the chronic one begins when the inflammatory scores reach a *plateau*, which should happen around the 15th day of treatment (Stolina *et al*. 2009, Bolon *et al*. 2011, Cascão *et al*. 2015, Vidal *et al*. 2015). By looking at figure IV.10, panel A, we can see that the treatment was finished in the second stage of disease's progression.

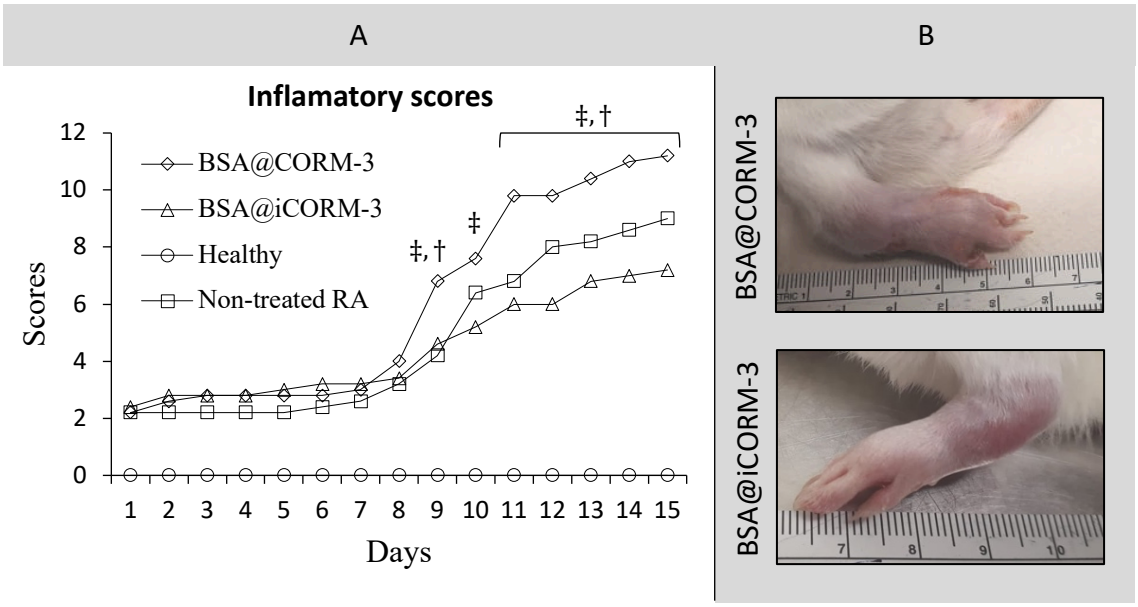

Figure IV.10. Visible state of the inflammation per group. (A) Daily inflammatory scores for each group assessed by the average of *N*. Mann-Whitney and Kruskal-Wallis tests were performed and differences were considered statistically significant for $P < .05$. (†) Non-treated RA vs. BSA@CORM-3 vs. BSA@iCORM-3, and (‡) BSA@CORM-3 vs. BSA@iCORM-3. (B) Left hind paw representative of the group's average inflammatory state (the ruler is in centimeters).

As mentioned before, RA is a chronic systemic inflammatory disease characterized by hyperproliferative cellular infiltration into the joints and high levels of proinflammatory cytokine expression, together leading to synovial hyperplasia and consequent bone and cartilage erosion (Cascão *et al*. 2014, Cascão *et al*. 2015). To illustrate such outcomes in the present model, histological images of left hind paws are displayed in figure IV.11.

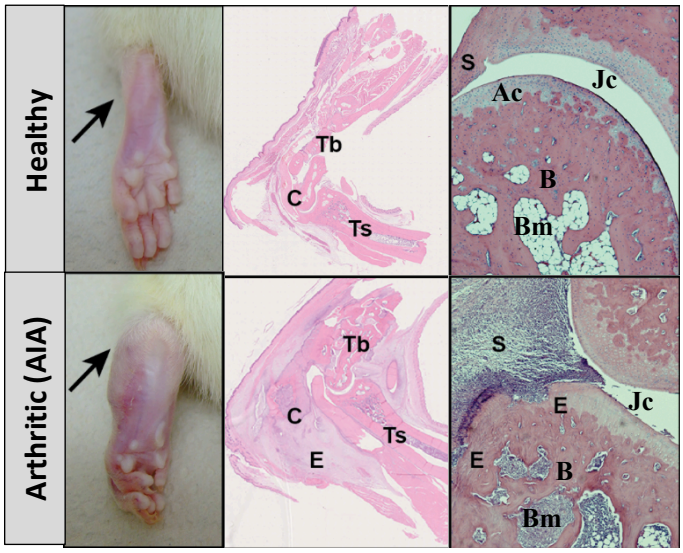

Figure IV.11. Illustrative histology of Winstar rats left hind paw, both healthy and with AIA, adapted from Cascão *et al.* (2015). Black arrows highlight the absence (Healthy) or presence (Arthritic) of swelling; Ac - articular cartilage, B - bone, Bm - bone marrow zones (with adipocytes, in Healthy, and immune cells, in Arthritic), C - calcaneus, E - erosion or edema, Jc - joint cavity, S - synovia, Tb - tibia and Ts - tarsus (Ac, B, Bm and Jc labels are not shown in the original).

Microscopic changes on cellular infiltration and erosion were also evaluated based on histological images such as the ones in figure IV.11, and the results represented in figure IV.12.

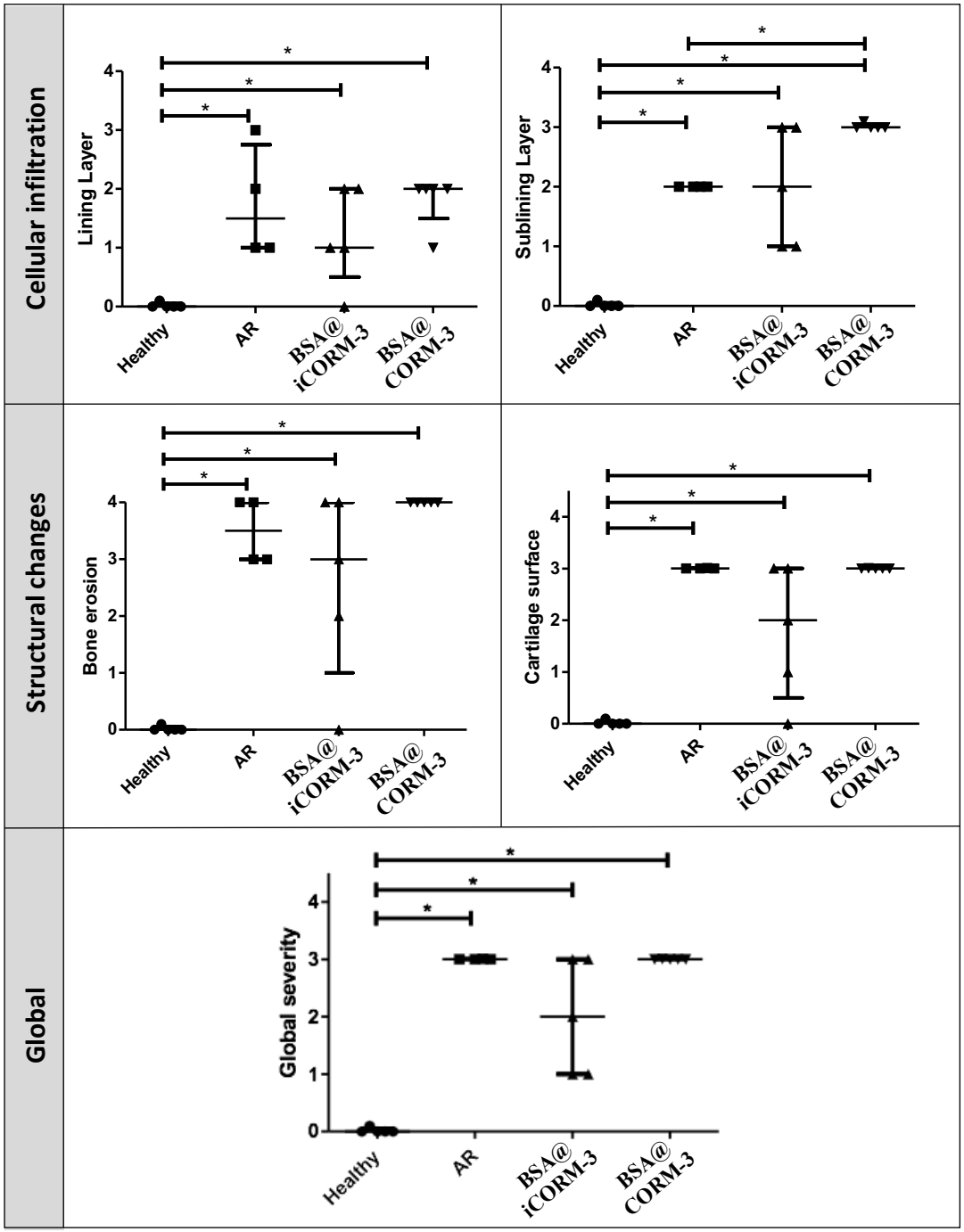

Figure IV.12. Semi-quantitative evaluation of histological sections. A Mann-Whitney test was performed and differences were considered statistically significant (*) for $P < .05$.

Although no previous evidence would suggest otherwise, all animal's liver, spleen and kidneys were visually healthy (not shown), qualitatively confirming the non-toxicity of the formulation.

The differences in the inflammatory scores shown in figure IV.10 between the non-treated RA group and both the BSA@CORM-3 and BSA@iCORM-3 were considered to be statistically not significant, suggesting a lack of effect of BSA@CORM-3 at this dose.

With the exception of a higher infiltration score in the sublining layer in figure IV.12, no other score was significantly higher in BSA@CORM-3 group. BSA@iCORM-3 group follows the same findings. The global severity graph clearly shows no histological differences found between the three RA-induced groups, which further confirms the lack of effect from BSA@CORM-3 at these conditions.

Finally, differences among BSA@iCORM-3 scores in figure IV.12 are higher when compared to other groups, as highlighted in the global graph. Interestingly, cellular infiltration in the lining layer and both structural changes assays show results identical to the healthy group control. Unexpectedly, differences between the inflammatory scores of the BSA@CORM-3 and BSA@iCORM-3 groups in figure IV.10, panel A, were considered to be statistically significant. Considering the lack of effects of iCORM-3 in previous studies together with the current results regarding BSA@CORM-3 ineffectiveness, these BSA@iCORM-3 results identical to the healthy group control in figure IV.12 would most likely be outliers, explaining a lack of macroscopic changes and overall inflammation in figure IV.10.

The more animals per group, the more confident one can be about results accuracy. With $N = 5$, it might be hard to draw definite conclusions, especially if there are outliers involved (or to "rigorously" show they are outliers - see Appendix 3, *Outliers*). Nonetheless, given the very low dosages and previous reports on CORM-3, biological variability is here considered to be the cause for the differences found between all RA-induced groups.

V. CONCLUSIONS AND FUTURE PERSPECTIVES

Protein-ligand interactions play an important role in drug's efficiency, especially considering albumin, which is a key transporter in blood (Ghuman *et al*. 2005). Therefore, two distinct spectroscopic approaches were performed in order to study such interactions between the carbonyl metal complex and BSA: UV-Vis spectroscopy and fluorescence quenching methods.

UV-Vis spectroscopy analysis suggests that CORM-3 interacts with the overall structure of BSA by exposing its aromatic amino acid residues (Trp, Tyr and Phe). Subsequent studies on the fluorescence quenching of BSA by this metal complex aimed at understanding the stability of such interactions.

A good linear Stern-Volmer relationship was obtained for the working range of protein and quencher concentrations. The obtained Stern-Volmer constants increase with increasing temperatures which suggests a dynamic quenching (Lakowicz 2006), *i.e.* collision of CORM-3 with tryptophan residues. However, the magnitudes are comparable to some static quenching reported in the literature (Lakowicz 2006, p. 282; Xu *et al*. 2013, Suryawanshi *et al*. 2016). Given Trp hydrophobic nature this could be explained by an increase in entropy during the complex formation between both moieties (Swadesh *et al*. 1987) or by CORM-3 decomposition itself. UV-Vis analysis confirmed the fast decomposition of the metal complex in the working buffer, with a degradation rate constant of 0.0026 s^{-1} and a half-life below 5 minutes. Given the fast loss of the ancillary ligand – gly – this could act as a second quencher, which would affect the Stern-Volmer constants. In order to test this last hypothesis further analysis in the presence of free gly should be performed.

By now, it has become clear that the fast decomposition kinetic of this particular CORM leads to difficulties in experimentally explore its interactions with biomolecules, since it becomes hard to differentiate CORM-3 actions from its ligand's, from its decomposition products'. Furthermore, it raises another question which is – given such fast decomposition, shouldn't its degradation products be studied instead? Other approaches could be used to further understand the forces behind such interaction with proteins, namely molecular docking.

It is fundamental to know a drug's *in vivo* outcome products prior to its commercialization. Consequently, the metal-CORMs decomposition and interaction with proteins needs further clarification if these class of molecules are to be used therapeutically.

The nanovectorization of CORM-3 in gold nanoparticles showed better anti-inflammatory efficiency in human monocytes than the delivery of the metal complex in

its free form. In the present work, it was proposed that the different cellular uptake between the AuNPs@PEG@BSA@CORM-3 and the free CORM-3 could explain their different anti-inflammatory efficiencies.

ICP-AES analysis showed levels of Ru below the LOD in cells treated with free CORM-3, whereas in the nanoconjugate assay Ru was detected and quantified in the first hours of incubation. Even so, discrepancies between those results and the supernatant ones point towards a poor cellular digestion at the time of sample preparation, which is not entirely strange considering cell matrixes' complexity and potential issues (Dykman *et al*. 2014, Matczuk *et al.* 2018).

Regardless, the analysis of the obtained supernatant values (a simpler matrix) suggest that ± 80 % of the total carbonyl metal complex added is internalized as free CORM-3, against ± 33 % as nanoconjugate. One important aspect is that, although cells were washed with water prior to the digestion, it cannot be excluded the possibility of some of the CORM-3 being in the cell membrane instead of inside the cell. Taking all into consideration, these results alone seem to leave open the explanation on why the AuNPs@PEG@BSA@CORM-3 had better anti-inflammatory efficiency when compared to free CORM-3. Still, the present assays should be repeated paying extra attention to cell matrixes digestion in the sample preparation steps.

In vivo assays are fundamental to assess the therapeutic viability of any drug. Hindrances on how far nanoconjugates can be concentrated in solution limits the possible dosages, so the theoretical maximum dose of CORM-3 delivered as AuNPs@PEG@BSA@CORM-3 was determined to be around ± 0.037 mg Kg^{-1}.

In vivo assays in arthritic (AIA) rats using a 0.037 mg Kg^{-1} CORM-3 dose, with BSA as a carrier in a 1:5 protein-to-ligand ratio, showed no anti-inflammatory effects. Given such outcome, the possibility of this particular nanoconjugate to be of practical use against Rheumatoid Arthritis, and probably to other systemic inflammatory disease, is very unlikely.

It is important to mention that CORM-3 is now mainly a model molecule for metal-based CORMs, with other CORMs showing better efficiencies and other non-metal-based CORMs being currently under development. Therefore, this nanoconjugate could be useful to deliver CORMs, particularly in localized inflammations. Regarding non-metal CORMs, photo-CORMs could be vectorized in this way and used to treat skin inflammations, and pH-dependent CORMs to treat stomach ulcers, just to give some examples.

Moreover, the ability to target the nanoconjugate through functionalization with peptides or sugars further extends the potential for AuNPs delivery of CORMs, not only to target inflammation but other diseases in which these molecules have already showed

therapeutic potential, namely in organ transplantation and preservation, and in cardiovascular diseases (Ling *et al*. 2017). Curiously, Ru-based CORMs even displayed antibacterial activity presumably by the metal center (Desmard *et al*. 2012), so could a nanoconjugate like the present one be used to target bacteria?

Although questions keep arising as novel insides are gathered about metal-CORMs nature, to date, the possible role of CORMs in medicine appear to be promising and rather versatile, explaining the high interest and need for further research.

VI. REFERENCES

Animal Models of Disease. Models of inflammation: Adjuvant-Induced Arthritis in the Rat. (2001). *Curr. Protoc. Pharmacol*. Supplement 13, pp. 5.5.1-5.5.5.

Bani-Hani, M. G., Greenstein, D., Mann, B. E., *et al*. (2006). Modulation of thrombin-induced neuroinflammation in BV-2 microglia by Carbon Monoxide-Releasing Molecule 3. *J. Pharmacol. Exp. Ther.*, 318(3), pp. 1315-1322.

Bento, M. L. and Tfouni, E. (1988) Spectra, reduction potencials, and coordinated pyrazine basicities in the ruthenium(II) complexes *trans*-$Ru(NH_3)_4LL'^{n+1}$. *Inorg. Chem.* 27, pp. 3410-3413.

Bergstraesser, C., Hoeger, S., Song, H., *et al*. (2012). Inhibition of VCAM-1 expression in endothelial cells by CORM-3: The role of the ubiquitin-proteasome system, p38, and mitochondrial respiration. *Free Radic. Biol. Med.*, 52(4), pp. 794-802.

Boczkowski, J., Poderoso, J. and Motterlini, R. (2006). CO–metal interaction: vital signaling from a lethal gas. *Trends Biochem. Sci.*, 31(11), pp.614-621.

Bolon, B., Stolina, M., King, C., *et al*. (2011). Rodent preclinical models for developing novel antiarthritic molecules: comparative biology and preferred method for evaluating efficacy. *J. Biomed. Biotechnol.*, 2011, pp. 1-21.

Bowman, S. and Bren, K. (2008). The chemistry and biochemistry of heme c: functional bases for covalent attachment. *Nat. Prod. Rep.*, 25(6), p.1118.

Brouard, S., Berberat, P., Tobiasch, E., *et al*. (2002) Heme Oxygenase-1-derived carbon monoxide requires the activation of transcription factor NF-B to protect endothelial cells from tumor necrosis factor-mediated apoptosis. *J. Biol. Chem.*, 277(20), pp. 17950-17961.

Bujacz, A. (2012) Structures of bovine, equine and leporine serum albumin. *Acta Cryst. D.* 68(10), pp. 1278-1289.

Cascão, R., Vidal, B., Lopes, I. P. *et al*. (2015). Decrease of CD68 synovial macrophages in Celastrol treated arthritic rats. *PLoS One*, 10(12), pp. 1-18.

Cascão, R., Vidal, B., Raquel, H. *et al*. (2014). Potent anti-inflammatory and proliferative effects of gambogic acid in rat model of antigen-induced arthritis. *Mediators Inflamm.*, pp. 1-7.

Chagas, M. A., Galvão, A. D., Moraes, F. T., *et al*. (2017). Synthesis, characterization and analysis of Leishmanicide ability of compound $[Ru(Cl)_3(H_2O)_2(gly)]$. *Open J. Inorg. Chem.* 7(4), pp. 89-101.

Chance, B., Erecinska, M. and Wagner, M. (1970). Mitochondrial responses to carbon monoxide toxicity. *Ann. NY Acad. Sci.*, 174(1 Biological Ef), pp.193-204.

Chang, L. and Karin, M. (2001). Mammalian MAP kinase signalling cascades. *Nature*, 410(6824), pp. 37-40.

Chaves-Ferreira, M., Albuquerque, I. S., Matak-Vinkovic, D., *et al*. (2015). Spontaneous CO Release from $Ru^{II}(CO)_2$-protein complexes in aqueous solution, cells, and mice. *Angew. Chem.*, 54(4), pp. 1172-1175.

Chen, Y., Zhang, F., Xu, C., *et al*. (2012). Theoretical investigation of water gas shift reaction catalyzed by iron group carbonyl complexes $M(CO)_5$ (M = Fe, Ru, Os). *J. Phys. Chem. A*, 116(10), pp. 2529-2535.

Chiang, N., Shinohara, M., Dalli, J., *et al*. (2013). Inhaled carbon monoxide accelerates resolution of inflammation via unique proresolving mediator-Heme Oxygenase-1 Circuits. *J. Immunol.*, 190(12), pp. 6378-6388.

Chow, M. K. and Zukoski, C. F. (1994). Gold sol formation mechanisms: role of colloidal stability. *J. Colloid Interface Sci.*, 165, pp. 97-109.

Clark, J. E., Naughton, P., Shurey, S., *et al*. (2003). Cardioprotective actions by a water-soluble carbon monoxide-releasing molecule. *Circ. Res.*, 93(2), pp. 1-7.

Cooper, C. and Brown, G. (2008). The inhibition of mitochondrial cytochrome oxidase by the gases carbon monoxide, nitric oxide, hydrogen cyanide and hydrogen sulfide: chemical mechanism and physiological significance. *J. Bioenerg. Biomembr.*, 40(5), pp.533-539.

Desmard, M., Foresti, R., Morin, D., *et al*. (2012). Differential antibacterial activity against pseudomonas aeruginosa by Carbon Monoxide-Releasing Molecules. *Antioxid. Redox Signal.* 16(2), pp. 153-163.

Dutra, F. and Bozza, M. (2014). Heme on innate immunity and inflammation. *Front. Pharmacol.*, 5, pp. 1-20.

Dykman, L. A. and Khlebtsov, N. G. (2014). Uptake of engineered gold nanoparticles into mammalian cells. *Chem Rev.,* 114(2), pp. 1258-1288.

Erratum: Carbon monoxide poisoning: pathogenesis, management, and future directions of therapy. (2017). *Am. J. Respir. Critical Care Medicine*, 196(3), pp.398-399.

Faa, G., Gerosa, C., Fanni, D., *et al*. (2018). Gold – Old drug with new potentials. *Curr. Med. Chem.* 25, pp. 75-84.

Fernandes, A. R., Jesus, J., Martins, P., *et al*. (2017). Multifunctional gold-nanoparticles: a nanovectorization tool for the targeted delivery of novel chemotherapeutic agents. *J. Control. Release*, 245, pp. 52-61.

Fernandes, A. R., Mendonça-Martins, I., Santos, M. F. A., *et al.* (2020). Improving the anti-inflammatory response via Gold nanoparticles vectorization of CO-Releasing Molecules. *ACS Biomater. Sci. Eng.*, 6(2), pp. 1090-1101.

Ferrándiz, M. L., Maicas, N., Garcia-Arnandis, I., *et al*. (2008). Treatment with CO-releasing molecule (CORM-3) reduces joint inflammation and erosion in murine collagen-induced arthritis. *Ann. Rheum. Dis.*, 67(9), pp. 1211-1217.

Floyd, M. A., Fassel, V. A., Winge, R. K., *et al*. (1980). Inductively coupled plasma-atomic emission spectroscopy computer controlled, scanning monochromator system for rapid sequential determination of the elements. *Anal. Chem.*, 52(3), pp. 431-438.

Fukuda, W., Takagi, T., Katada, K., *et al*. (2014). Anti-inflammatory effects of Carbon Monoxide-Releasing Molecule on trinitrobenzene sulfonic acid-induced colitis in mice. *Dig. Dis. Sci.*, 59(6), pp. 1142-1151.

Ghuman, J., Zunszain, P. A., Petitpas, I., *et al*. (2005). Structural basis of the drug-binding specificity of Human Serum Albumin. *J. Mol. Biol.* 353(1), pp. 38-52.

Gray, H. B. and Beach, N. A. (1963) The electronic structures of octahedral metal complexes. I. Metal Hexacarbonyls and Hexacyanides. *J. Am. Chem. Soc.* 85(19), pp. 2922-2927.

Groch, M. W. (1998). Radioactive decay. *J. Imaging. Sci.* 18(5), pp. 1247-1256.

Hegazi, R. A. F., Rao, K. N., Mayle, A., *et al*. (2005). Carbon monoxide ameliorates chronic murine colitis through a heme oxygenase 1-dependent pathway. *J. Exp. Med.*, 202(12), pp. 1703-1713.

Holdsworth, S. R. and Gan, P-Y. (2015). Cytokines: names and numbers you should care about. *Clin. J. Am. Soc. Nephrol.*, 10(12), pp. 2243-2254.

Housecroft, C. and Sharpe, A. (2005). *Inorganic chemistry (2a. ed.)*. Harlow: Pearson Educación.

Hu, Y. J., Liu, Y., Wang, J. B., *et al*. (2004) Study of the interaction between monoammonium glycyrrhizinate and bovine serum albumin. *J. Pharm*. *Biomed*. *Anal*. 36(4), 915-919.

Ibáñez, L., Alcaraz, M. J., Maicas, N., *et al*. (2012). Downregulation of the inflammatory response by CORM-3 results in protective effects in a model of postmenopausal arthritis. *Calcif. Tissue Int.*, 91(1), pp. 69-80.

Ismailova, A., Kuter, D., Bohle, D. S., *et al*. (2018). An overview of the potential therapeutic applications of CO-Releasing Molecules. *Bioinorg. Chem. Appl.*, 2018, pp. 1-23.

Jeffrey, K. L., Camps, M., Rommel, C., *et al*. (2007). Targeting dual-specificity phosphatases: manipulating MAP kinase signalling and immune responses. *Nat. Rev. Drug Discov.*, 6, pp. 391-403.

Joe, B., Grittiths, M. M., Remmers, E. F. *et al*. (1999). Animal models of rheumatoid arthritis and related inflammation. *Curr. Rheumatol. Rep.*, 1(2), pp. 139-148.

Johnson, G. L. and Nakamura, K. (2007). The c-jun kinase/stress-activated pathway: regulation, function and role in human disease. *Biochim. Biophys. Acta*, 1773(8), pp. 1341-1348.

Kapturczak, M. H., Wasserfall, C., Brusko, T., *et al*. (2004). Heme Oxygenase-1 modulates early inflammatory responses. *Am. J. Pathol.*, 165(3), pp. 1045-1053.

Kim, H. P., Wang, X., Zhang, J., *et al*. (2005). Heat Shock Protein-70 mediates the cytoprotective effect of carbon monoxide: involvement of p38 MAPK and Heat Shock Factor-1. *J. Immunol.*, 175(4), pp. 2622-2629.

Kong, D-H., Kim, Y. K., Kim, M. R., *et al*. (2018). Emerging roles of vascular cell Adhesion Molecule-1 (VCAM-1) in immunological disorders and cancer. *Int. J. Mol. Sci.*, 19(4), pp. 1-16.

Kong, F-Y., Zhang, J-W., Li, R-F., *et al*. (2017). Unique roles of gold nanoparticles in drug delivery, targeting and imaging applications. *Molecules*, 22(9), pp. 1-13.

Kumar, L. D., Karthik, R., Gayathri, N., *et al*. (2016). Advancement in contemporary diagnostic and therapeutic approaches for rheumatoid arthritis. *Biomed. Pharmacother.*, 79, 52-61.

Laidler, K. J. (1984). The development of the Arrehnius equation. *J. Chem. Ed.* 61(6), pp. 494-498.

Lakowicz, J. R. (2010). *Principals of Fluorescence Spectroscopy (3rd ed).* Springer

Larsen, R., Gouveia, Z., Soares, M. *et al*. (2012). Heme cytotoxicity and the pathogenesis of immune-mediated inflammatory diseases. *Front. Pharmacol.*, 3.

Lee, P. C. and Meisel, D. (1982). Adsorption and surface-enhanced Raman of dyes on silver and gold sols. *J. Phys. Chem.*, 86(17), pp. 3391-3395.

Leike, A. (2002). Demonstration of the exponential decay law using beer froth. *Eur. J. Phys.* 23, 21-26.

Ley, K., Laudanna, C., Cybulsky, M. *et al*. (2007). Getting to the site of inflammation: the leykocyte adhesion cascade update. *Nat. Rev. Immunol.,* 7(9), pp. 678-689.

Lin, Q., Weis, S., Yang, G., Weng, Y-H., *et al*. (2007). Heme Oxygenase-1 protein localizes to the nucleus and activates transcription factors important in oxidative stress. *J. Biol. Chem*. 282(28), pp. 20621-20633.

Ling, K., Men, F., Wang, W.-C., *et al*. (2017). Carbon Monoxide and its controlled release: therapeutic application, detection, and development of Carbon Monoxide Releasing Molecules (CORMs). *J. Med. Chem.*, 61(7), pp. 2611-2635.

Lopez-Chaves, C., Soto-Alvaredo, J., Montes-Bayon, M., *et al*. (2018). Gold-nanoparticles: distribution, bioaccumulation and toxicity. In vitro and in vivo studies. *Nanomedicine*, 14(1), pp. 1-12.

Maicas, N., Ferrándiz, M. L., Devesa, I., *et al*. (2010). The CO-releasing molecule CORM-3 protects against articular degradation in the K/BxN serum transfer arthritis model. *Eur. J. Pharmacol.*, 634(1-3), pp. 184-191.

Maines, M. (1997). The heme oxygenase system: a regulator of second messenger gases. *Annu. Rev. Pharmacol. Toxicol.*, 37, pp. 517-554.

Maines, M. D., Trakshel, G. M. and Kutty R. K. (1986). Characterization of two constitutive forms of rat liver microsomal heme oxygenase. *J. Biol. Chem.*, 261(1), pp.411-419.

Mann, B. and Motterlini, R. (2007). CO and NO in medicine. *ChemComm*, 41, pp. 4197-4208.

Matczuk, M., Ruzik, L., Aleksenko, S., *et al*. (2018). Analytical methodology for studying cellular uptake, processing and localization of gold nanoparticles. *Anal. Chim. Acta.* 1052, pp.1-9.

McInnes, I. B. and Schett, G. (2011). The pathogenesis of rheumatoid arthritis. *N. Engl. J. Med.*, 365(23), pp. 2205-2219.

McLean, S., Mann, B. R. and Poole, R. K. (2012). Sulfite species enhanced carbon monoxide release from CO-releasing molecules: Implications for the deoxymyoglobin assay of activity. *Anal. Biochem.*, 427(1), pp. 36-40.

Morita, T., Perrella, M. A., Lee, M-E., *et al*. (1995). Smooth muscle cell-derived carbon monoxide is a regulator of vascular cGMP. *Proc. Natl. Acad. Sci. U.S.A*, 92(5), pp. 1475-1479.

Morse, D., Pischke, S. E., Zhou, Z., *et al*. (2003). Supression of inflammatory cytokine production by carbon monoxide involves the JNK pathway and AP-1. *J. Biol. Chem.*, 278, pp. 36993-36998.

Motterlini, R., Mann, B. E., Johnson, *et al*. (2003). Bioactivity and pharmacology actions of Carbon Monoxide-Releasing Molecules. *Curr. Pharm. Des.*, 9(30), pp. 2525-2539.

Motulsky, H. J. and Brown, R. E. (2006) Detecting outliers when fitting data with nonlinear regression – a new method based on robust nonlinear regression and the false discovery rate. *BMC Bioinformatics.* 7, pp. 1-20.

Naik, K. M. and Nandibewoor, S. T. (2013). Spectral characterization of the binding and conformational changes of bovine serum albumin upon interaction with an anti-fungal drug, methylparaben. *Spectrochim. Acta A Mol. Biomol. Spectrosc.* 105, pp. 418-423.

Nakao, A., Moore, B. A., Murase, N., *et al*. (2003). Immunomodulatory effects of inhaled carbon monoxide on rat syngeneic small bowel graft motility. *Gut*, 52(9), pp. 1278-1285.

Nakao, A., Neto, J. S., Kanno, S., *et al*. (2005). Protection against ischemia/reperfusion injury in cardiac and renal transplantation with carbon monoxide, biliverdin and both. *Am. J. Transplant.*, 5(2), pp. 282-291.

Orellano, T., Dergal, E., Alijani, M., *et al*. (1976). Studies on the mechanism of carbon monoxide toxicity. *J. Surg. Res.*, 20(5), pp.485-487.

Otterbein, L. E., Bach, F. H., Alam, J., *et al*. (2000). Carbon monoxide has anti-inflammatory effects involving the mitogen-activated protein kinase pathway. *Nat. Med.*, 6(4), pp. 422-428.

Otterbein, L., Foresti, R. and Motterlini, R. (2016). Heme Oxygenase-1 and carbon monoxide in the heart. *Circ. Res.*, 118(12), pp.1940-1959.

Panahi, Y., Mohammadhosseini, M., Nejati-Koshki, K., *et al*. (2017). Preparation, surface properties, and therapeutic applications of gold nanoparticles in biomedicine. *J. Drug Res.*, 67(2), pp. 77-87.

Pober, J. S. (2002). Endothelial activation: intracellular signaling pathways. *Arthritis Res. Ther.*, 4(Suppl 3), pp. S109-S116.

Poss, K. and Tonegawa, S. (1997a). Reduced stress defense in heme oxygenase 1-deficient cells. *Proc. Natl. Acad. Sci. U.S.A*, 94, pp. 10925-10930.

Poss, K. and Tonegawa, S. (1997b). Heme oxygenase 1 is required for mammalian iron reutilization. *Proc. Natl. Acad. Sci. U.S.A*, 94, pp. 10919-10924.

Pretsch, E., Buhlmann, P. and Badertscher, M. (2009). *Structure Determination of Organic Compounds. Tables of Spectral Data. (4th ed.)*. Springer.

Puckett, C. A. and Barton, J. K. (2008). Mechanism of cellular uptake of a ruthenium polypyridyl complex. *Biochemistry*, 47(45), pp. 11711-11716.

Ralle, M. and Lutsenko, S. (2009). Quantitative imaging of metals in tissues. *BioMetals*. 22(1), pp. 197-205.

Raposo, L. R., Roma-Rodrigues, C., Jesus, J., *et al*. (2017). Targeting canine mammary tumours via gold nanoparticles functionalized with promising Co(II) and Zn(II) compounds. *Vet. Comp. Oncol.*, 15(4), pp. 1537-1542.

Reger, D. L., Goode, S. R., Mercer, E. E. *et al*. (1997). *Química: Princípios e Aplicações. (1st ed.).* Fundação Calouste Gulbenkian.

Romão, C. C., Blattler, W. A., Seixas, J. D. *et al*. (2012). Developing drug molecule for therapy with carbon monoxide. *Chem. Soc. Rev.*, 41(9), pp. 3571-3583.

Rose, J. J., Wang, L., Xu, Q., *et al*. (2016). Carbon monoxide poisoning: pathogenesis, management, and future directions of therapy. *Am. J. Respir. Crit. Care Med.* 196(5), pp. 596-606.

Santos-Silva, T., Mukhopadhyay, A., Seixas, J. D., *et al*. (2011). CORM-3 reactivity toward Proteins: the crystal structure of a Ru(II) dicarbonyl-lysozyme complex. *J. Am. Chem. Soc.*, 133(5), pp. 1192-1195.

Sawle, P., Foresti, R., Mann, B. E., *et al*. (2005). Carbon monoxide-releasing molecules (CO-RMs) attenuate the inflammatory response elicited by lipopolysaccharide in RAW264.7 murine macrophages. *Br. J. Pharmacol.*, 145(6), pp. 800-810.

Schatzschneider, U. (2015). Novel lead structures and activation mechanisms for CO-releasing molecules (CORMs). *Br. J. Pharmacol.*, 172(6), pp. 1638-1650.

Schmid, F.-X. (2001). Biological macromolecules: UV-visible spectrophotometry. *Encyclopedia of Life Sciences.* pp. 1-4.

Schultz, E. (1997). Dice-shaking as an analogy for radioactive decay and first order kinetics. *J. Chem. Educ.* 74(5), pp. 505-507.

Schulz, H., Gorling, A. and Hieringer, W. (2013). Mechanisms of the water-gas shift reaction catalyzed by ruthenium pentacarbonyl: a density functional theory study. *Inorg. Chem.*, 52(9), pp. 4786-4794.

Seixas, J. D., Santos, M. F. A., Mukhopadhyay, A. *et al*. (2014). A contribution to the rational design of $Ru(CO)_3Cl_2L$ complexes for *in vivo* delivery of CO. *Dalton Trans.* 44(11), pp. 5058-5075.

Sekula, B., Zielinski, K. and Bujacz, A. (2013) Crystallographic studies of the complexes of bovine and equine serum albumin with 3,5-diiodosalicylic acid. *Int. J. Biol. Macromol.* 60, pp. 316-324.

Serizawa, F., Patterson, E., Potter, *et al*. (2015). Pretreatment of human cerebrovascular endothelial cells with CO-Releasing Molecule-3 interferes with JNK/AP-1 signaling and suppresses LPS-induced proadhesive phenotype. *Microcirculation*, 22(1), pp. 28-36.

Sjöstrand, T. (1949). Endogenous formation of carbon monoxide in man. *Nature*, 164(4170), pp.580-581.

Spencer, A., Bagai, I., Becker, D., *et al*. (2014). Protein/protein interactions in the mammalian heme degradation pathway. *J. Biol. Chem.*, 289(43), pp.29836-29858.

Sperling, R. A., Gil, P. R., Zhang, F. *et al*. (2008) Biological applications of gold nanoparticles. *Chem. Soc. Rev.*, 37(9), pp. 1896-1908.

Stepic, R., Wick, C. R., Strobel, V., *et al*. (2019). Mechanism of the water-gas shift reaction catalyzed by efficient ruthenium-based catalysts: a computational and experimental study. *Angew. Chem.*, 58(3), pp. 741-745.

Stolina, M., Bolon, B., Middleton, S. *et al*. (2009). The evolving systemic and local biomarker milieu at different stages of disease progression in rat adjuvant-induced arthritis. *J. Clin. Immunol.*, 29(2), pp. 158-174.

Suryawanshi, V. D., Walekar, L. S., Gore, A. H., *et al*. (2016) Spectroscopic analysis on the binding interaction of biologically active pyrimidine derivative with bovine serum albumin. *J. Pharm. Biomed. Anal.* 6(1), pp. 56-63.

Swadesh, J. K., Mui, P. W. and Scheraga, H. A. (1987). Thermodynamics of the quenching of tyrosyl fluorescence by dithiothreitol. *Biochemistry.*, 26(18), pp. 5761-5769.

Takagi, T., Naito, Y., Inoue, M., *et al*. (2009). Inhalation of carbon monoxide ameliorates collagen-induced arthritis in mice and regulates the articular expression of IL-1 and MCP-1. *Inflammation*, 32(2), 83-88.

Tenhunen, R., Marver, H. and Schmid, R. (1968). The enzymatic conversion of heme to bilirubin by microsomal heme oxygenase. *Proc. Nat. Acad. Sci. U.S.A*, 61(2), pp.748-755.

Tenhunen, R., Ross, M., Marver, H. and Schmid, R. (1970). Reduced nicotinamide adenine dinucleotide phosphate dependent biliverdin reductase. Partial purification and characterization. *Biochemistry*, 9(2), pp.298-303.

Thom, S., Bhopale, V., Han, S., *et al*. (2006). Intravascular neutrophil activation due to carbon monoxide poisoning. *Am. J. Respir. Crit.*, 174(11), pp.1239-1248.

Tornatore, L., Thotakura, A. K., Bennet, J., *et al*. (2012). The nuclear factor kappa B signaling pathway: integrating metabolism with inflammation. *Trends Cell Biol.*, 22(11), pp. 557-566.

Townsend, M. J. (2014). Molecular and cellular heterogeneity in the rheumatoid arthritis synovium: clinical correlates of synovitis. *Best Pract. Res.: Clin. Rheumatol.*, 28(4), pp. 539-549.

Tsui, T-Y., Siu, Y-T., Schlitt, H. J. *t al*. (2005). Heme oxygenase-1-derived carbon monoxide stimulates adenosine triphosphate generation in human hepatocyte. *Biochem. Biophys. Res. Commun.*, 336(3), pp. 898-902.

Urquhart, P., Rosignoli, G., Cooper, D., *et al*. (2007). Carbon Monoxide-Releasing Molecules modulate leukocyte-endothelial interactions under flow. *J. Pharmacol. Exp. Ther.*, 321(2), pp. 656-662.

Veigas, B., Matias, A., Calmeiro, T., *et al*. (2019). Antibody modified gold nanoparticles for fast colorimetric screening of rheumatoid arthritis. *Analyst*, 11, pp. 1-8.

Verma, A., Hirsch, D., Glatt, C., *et al*. (1993). Carbon monoxide: a putative neural messenger. *Science*, 259, pp. 381-384.

Vidal, B., Cascão, R., Vale, A. C. (2015). Arthritis induces early bone high turnover, structural degradation and mechanical weakness. *PLoS One*, 10(1), pp. 1-10.

Vile, G. F., Basu-Modak, S., Waltner, C. *et al*. (1994). Heme oxygenase 1 mediates an adaptative response to oxidative stress in human skin fibroblasts. *Proc. Nat. Acad. Sci. U.S.A*, 91, pp. 2607-2610.

Wang, R., Wu, L. and Wang, Z. (1997). The direct effect of carbon monoxide on K_{Ca} channels in vascular smooth muscle cells. *Pflugers Arch.*, 434(3), pp. 285-291.

Wegiel, B., Hanto, D. W. and Otterbein, L. E. (2013). The social network of carbon monoxide in medicine. *Trends Mol. Med*., 19(1), PP. 3-11.

Williams, M. A. and Daviter, T. (2013). *Protein-Ligand Interactions. Methods and Applications (2nd ed).* Springer.

Xu, H., Yao, N., Xu, H. *et al*. (2013). Characterization of the interaction between eupatorin and bovine serum albumin by spectroscopic and molecular modeling methods. *Int. J. Mol. Sci.* 14, pp. 14185-14203.

Yachie, A., Niida, Y., Wada, T., *et al*. (1999). Oxidative stress causes enhanced endothelial cell injury in human heme oxygenase-1 deficiency. *J. Clin. Invest.*, 103(1), pp. 129-135.

Yeh, A. and Taube, H. (1980). Acid hydrolysis of ethyl glycinate complex of Pentaammineruthenium(III). *J. Am. Chem. Soc.* 102, pp. 4725-4729.

Zhang, L., Zhang, Y., Zhong, W., *et al*. (2014). Heme Oxygenase-1 ameliorates dextran sulfate sodium-induced acute murine colitis by regulating Th17/treg cell balance. *J. Biol. Chem.*, 289(39), pp. 26847-26858.

Zhang, X., Shan, P., Alam, J., *et al*. (2003). Carbon monoxide modulates Fas/Fas ligand, caspases, and Bcl-2 family proteins via the p38 mitogen-activated protein kinase pathway during ischemia-reperfusion lung injury. *J. Biol. Chem.*, 278(24), pp. 22061-22070.

APPENDICES

Appendix 1

HSA and BSA Homology

Structural homology was determined between A chains of both proteins, using jFATCAT - rigid algorithm from rcsb.org (PDB IDs: 2BX8 and 3V03).

Sequence homology was determined using the Align Sequence Protein BLAST tool from uniprot.org (FASTA files were exported from entries P02768 and P02769).

Data Normalization

The absorbance values were normalized between 0 and 1 using the equation A.1 bellow.

$$(A.1) \quad A' = \frac{A - A_{minimum}}{A_{maximum} - A_{minimum}}$$

UV-Vis Interaction Analysis

Spectra at 10 min, 1 and 24 h incubations overlapped have little to none differences, as can be seen in figure A.1., by taking three different ratios as examples.

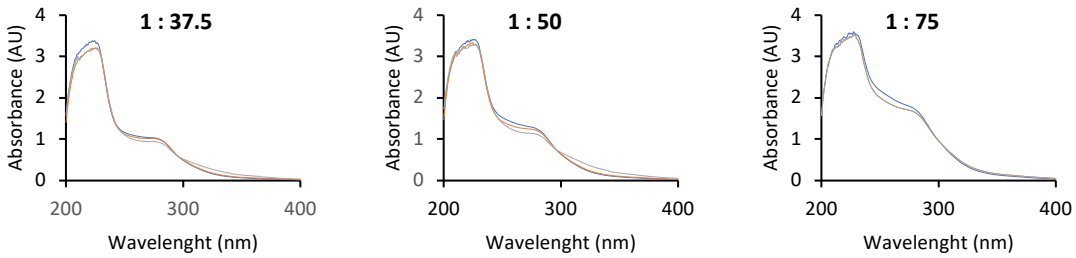

Figure A.1. UV-Vis spectra for different incubation times (10 min in blue, 1h in orange and 24 h in gray) overlapped by BSA:CORM-3 ratios.

Fluorescence Intensity vs. Wavelength

The raw data for BSA quenching by CORM-3 is displayed in figure A.2. below. The highest fluorescence emission in each assay belong to free BSA.

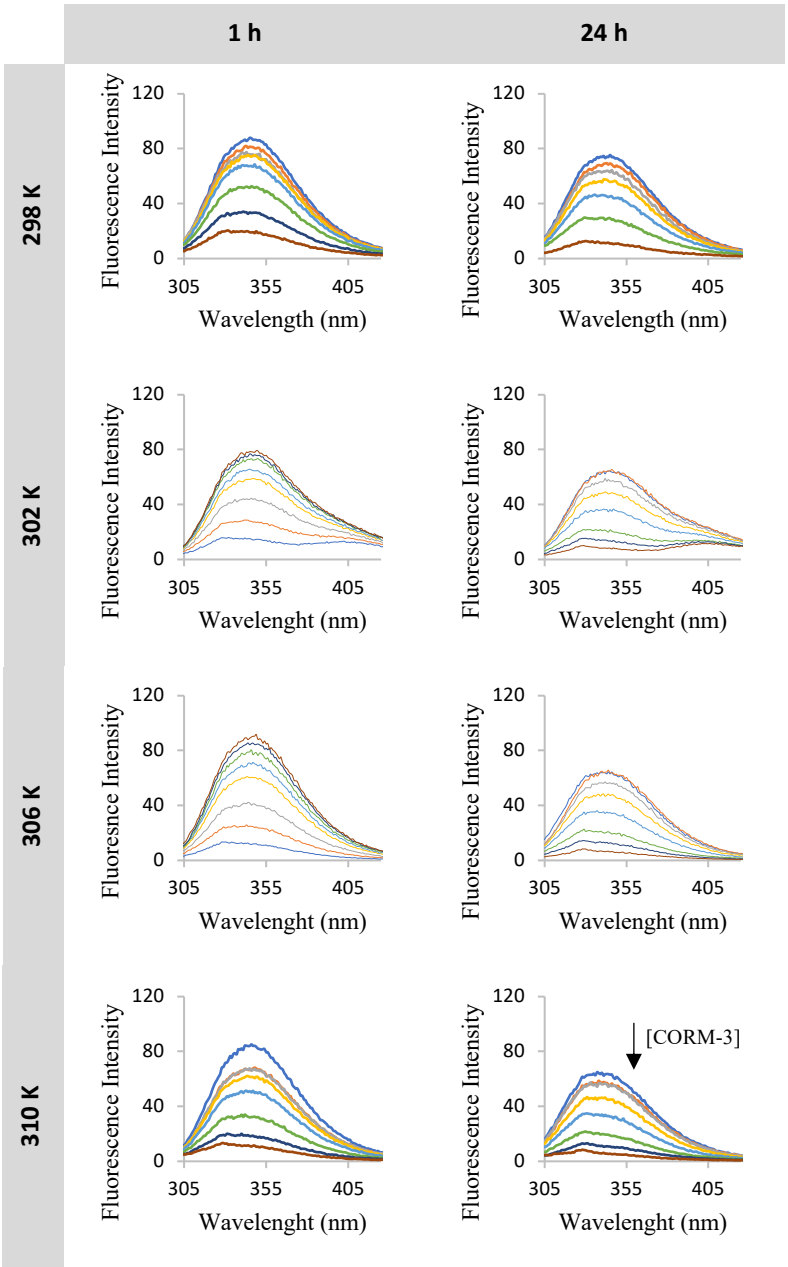

Figure A.2. Emission spectra of a constant concentration of BSA, with and without CORM-3, following the excitation at 295 nm, at different temperatures (298, 302, 306 and 310 K) for different incubation times (10 min, 1 h and 24 h). Black arrow highlights the increasing concentrations of CORM-3 (0 to 100 µM).

ln K vs. 1/T

By plotting the ln ("K_{SV}") against 1/T a linear fit is obtained:

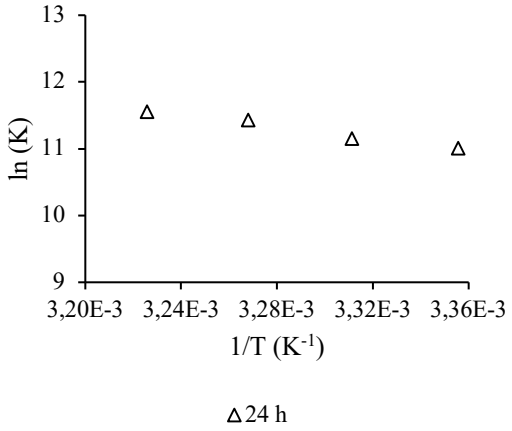

Figure A.3. Van't Hoff plot using the Stern-Volmer experimental constants at 24h.

If K_{SV} is an *equilibrium* constant, then the Van't Hoff equation (IV.5) arises as a prediction of the thermodynamic parameters behind fluorophore and quencher interaction.

Considering the ideal gas constant (≈ 8.314 J K^{-1} mol^{-1}), ΔH^0 can be taken from the slope of the regression and ΔS^0 by the y-intercept. Furthermore, the standard free energy, ΔG^0, could then be calculated from equation A.2. (Swadesh *et al*. 1987):

$$\Delta G^0 = \Delta H^0 - T\Delta S^0 \quad \text{(A.2)}$$

All things considered, if K_D was in fact a K_{SV}, then these thermodynamic parameters would be as in the table A.1. below:

Table A.1. Thermodynamic parameters assuming a static quenching, K_{SV}.

time	R^2	ΔH^0 (KJ mol^{-1})	ΔS^0 (J K^{-1} mol^{-1})	ΔG^0 (KJ mol^{-1})
24 h	0.9768	36,57	214,19	-27,25

Although such linearity might be convincing, it should not be forgotten that an identical linear relationship is obtained by the linearization (A.3) of the Arrhenius equation, which describes a *rate* constant dependence on temperature (recall, $K_D = k_d \times \tau_0$):

$$\ln(K) = \ln A - \frac{E_a}{R}\frac{1}{T}, \quad \text{(A.3)}$$

that is, a ln (K) vs. 1/T plot (Laidler 1984).

In conclusion, a $\Delta S^0 > 0$ doesn't rule out a static mechanism for Stern-Volmer constants increasing with temperature but doesn't prove one either. $\Delta S^0 < 0$ always mean a static quenching and K_{SV} would decrease with increasing temperatures (Swadesh *et al* 1987, Xu *et al*. 2013, Suryawanshi *et al*. 2016).

Appendix 2

Nanoconjugates Characterization

In order to confirm functionalization, two different assays were performed after each step: PEG and BSA quantification in the excess solutions (figure A.4.), and assessment of the nanoconjugate sizes by DLS analysis (table A.2.).

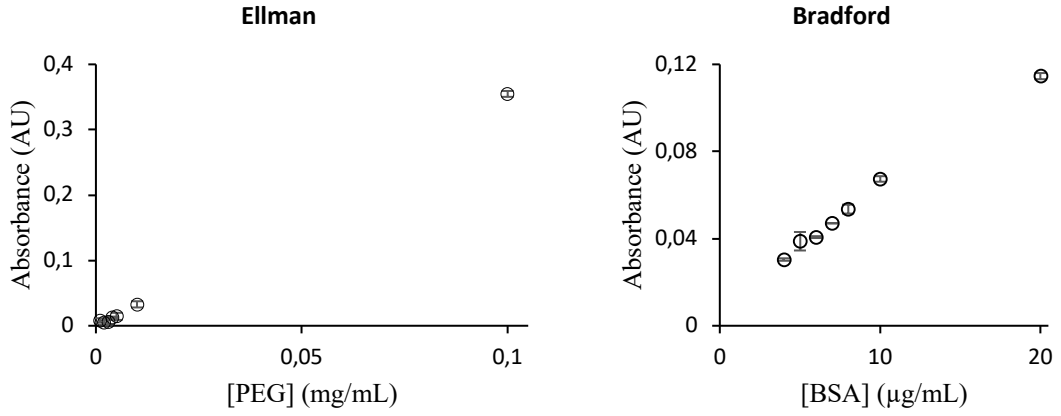

Figure A.4. Linear standard curves for AuNPs functionalization, with error bars corresponding to SDs. (Left) Ellman's assay quantification of free thiols (-SH). The linear range is given by $Abs_{412\ nm}$ = 3.5614 [PEG] – 0.0016, with $R^2 \cong 0.999$. (Right) Bradford's assay quantification of protein. The linear range is given by $Abs_{595\ nm}$ = 0.0052 [BSA] + 0.0112, with $R^2 \cong 0.995$.

All PEG in solution was added to the AuNPs ($Abs^{PEG}_{exc.\ sol.}$ = - 0.004 ± 0.002), whereas 0.011 µg mL^{-1} of BSA was quantified ($Abs^{BSA}_{exc.\ sol.}$ = 0.0037 ± 0.0002), meaning that around 50% of the BSA in solution was added to the AuNPs@PEG.

As displayed below in table A.2., further DLS measurements confirmed the functionalization.

Table A.2. Dynamic Light Scattering analysis of the nanoconjugates, both the Z-Average (or hydrodynamic diameter, in nm) and PI (Polydispersity Index), as means ± SD.

DLS	AuNPs	AuNPs@PEG	AuNPs@PEG@BSA	AuNPs@PEG@BSA@CORM3
nm	19.4 ± 1.1	22.0 ± 1.3	40.9 ± 0.6	82.1 ± 10.1
PI	0.135 ± 0.111	0.157 ± 0.132	0.460 ± 0.030	0.602 ± 0.088

As expected, the hydrodynamic diameter increases after each preparation step. Polydispersity Indexes (PI) suggest that AuNPs and AuNPs@PEG are monodisperse solutions (< ± 0.25), but AuNPs@PEG@BSA and AuNPs@PEG@BSA@CORM-3 are polydisperse (> ± 0.25). These results are consistent considering that the higher the degree of functionalization, less likely it is to obtain uniform nanoconjugates in solution.

Considering Pellet Values

Since ICP-AES was able to quantify Au and Ru within cells in the nanoconjugate assay, table A.3. display the amount of Ru and AuNPs determined based on those results.

Table A.3. Ru (in µmol) and AuNP (in nmol) determination in both fractions based on the values given in table IV.2.

[AuNP@...@CORM3]	**8 nM** (meaning 2 µM of CORM-3)					
Element	**Ruthenium**			**AuNP**		
Incubation time	**1 h**	**3 h**	**6 h**	**1 h**	**3 h**	**6 h**
Supernatant (µmol | nmol)	6.53×10^{-3}	6.53×10^{-3}	$7{,}12\times10^{-3}$	2.11×10^{-2}	2.04×10^{-2}	$2{,}26\times10^{-2}$
Pellet (µmol | nmol)	$1{,}58\times10^{-4}$	$2{,}08\times10^{-4}$	< LOD	$3{,}42\times10^{-3}$	$4{,}68\times10^{-3}$	$7{,}54\times10^{-3}$
Supernatant (%)	98	97	-	86	81	75
Pellet (%)	2	3	-	14	19	25

Considering these values, the internalization of nanoconjugate is lower than if considering only the supernatant ones (see table IV.4), which is in agreement with the previous suggestion of a poor cell matrixes digestion.

The fact that Ru wasn't detected only in the pellet of the 6 h incubation (< LOD), when the other results suggest similar amounts as in the 1 and 3 h assays, further strengthens the hypothesis of problems in these samples preparation.

Appendix 3

Dose Rationale

Rats weight ± 200 g, so a 10 mg Kg^{-1} dose of CORM-3 would mean

$$10\ \text{mg} - 1\ 000\ 000\ \text{mg}$$
$$\text{x mg} - 200\ 000\ \text{mg}$$
$$\text{x} = 2.0\ \text{mg} = 0.002\ \text{g}$$
$$\frac{0.002\ \text{g}}{294.61\ \text{g/mol}} \cong 6.789 \times 10^{-6}\ \text{mol}$$

0.002 g of metal complex, or 6.789×10^{-6} mol ($MW_{CORM\text{-}3}$ = 294.61 g mol^{-1}). The ratio between species in the AuNP@PEG@BSA@CORM-3 nanoconjugate are 1:1450:6:254, respectively (Fernandes *et al.* 2020). Assuming such ratios,

$$1 \quad - \quad 254$$
$$\text{y mol} \quad - \quad 6.789 \times 10^{-6}\ \text{mol}$$
$$\text{y} \cong 2.6764 \times 10^{-8}\ \text{mol} = 26.764\ \text{nmol}$$

it would be needed a 26 764 nM AuNP@PEG@BSA@CORM-3 injection to meet a 10 mg Kg^{-1} dose of CORM-3.

Considering such impossibility, a theoretical limit concentration of nanoconjugate is set at 100 nM. For this imposed value:

$$1\ \text{nM} - 0{,}25\ \mu\text{M}$$
$$100\ \text{nM} - \text{z}\ \mu\text{M}$$
$$\text{z} = \ 25\ \mu\text{M}$$
$$25\ \mu\text{M} = \frac{\text{n}}{0.001\ \text{L}} \Leftrightarrow \text{n} = 0.025\ \mu\text{mol} = 2.5 \times 10^{-8}\ \text{mol}$$
$$2.5\ \times\ 10^{-8}\ \text{mol}\ \times\ 294.61\ \text{g/mol} \cong\ 7.365 \times 10^{-6}\ \text{g}$$
$$\frac{7.365 \times 10^{-3}\ \text{mg} \times\ 1\ \text{Kg}}{0.2\ \text{Kg rat}}\ \cong 0.0368\ \text{mg}$$

the possible dose to be administrated using AuNP@PEG@BSA@CORM-3 is 0.0368 mg Kg^{-1} of CORM-3, which is less than 4 % of the initially proposed upper dose (10 mg Kg^{-1}) and, of course, less than 8 % of the lower (5 mg Kg^{-1}).

Outliers

Since outliers are not generated by any predicted model, any method for their detection has to be somewhat arbitrary and there are different methods used to identify such values. As an attempt to formally show the existent of outliers in the BSA@iCORM-3 group, the individuals inflammatory scores were subject to the ROUT test using GraphPad Prism.

The test wasn't able to identify any outlier from the data set from each day. Although this method can theoretically detect an outlier within a set of $N > 3$, it struggles to find the ones that are not "too obvious", as in the present data sets (Motulsky *et al*. 2006).